

The DESI One-Percent Survey: Exploring A Generalized SHAM for Multiple Tracers with the UNIT Simulation

Jiayi Yu,¹★ Cheng Zhao,^{2,1}† Violeta Gonzalez-Perez,^{3,4} Chia-Hsun Chuang,⁵ Allyson Brodzeller,⁵ Arnaud de Mattia,⁶ Jean-Paul Kneib,^{1,7} Alex Krolewski,^{8,9,10} Antoine Rocher,⁶ Ashley Ross,¹¹ Yunchong Wang,^{12,13} Sihan Yuan,^{12,14} Hanyu Zhang,¹⁵ Rongpu Zhou,¹⁶ Jessica Nicole Aguilar,¹⁶ Steven Ahlen,¹⁷ David Brooks,¹⁸ Kyle Dawson,⁵ Alex de la Macorra,¹⁹ Peter Doel,¹⁸ Kevin Fanning,^{11,20} Andreu Font-Ribera,²¹ Jaime Forero-Romero,²² Satya Gontcho A Gontcho,¹⁶ Klaus Honscheid,^{11,20} Robert Kehoe,²³ Theodore Kisner,¹⁶ Anthony Kremin,¹⁶ Martin Landriau,¹⁶ Marc Manera,^{21,24} Paul Martini,^{25,11} Aaron Meisner,²⁶ Ramon Miquel,^{21,27} John Moustakas,²⁸ Jundan Nie,²⁹ Will Percival,^{9,10,8} Claire Poppett,^{16,30,31} Anand Raichoor,¹⁶ Graziano Rossi,³² Hee-Jong Seo,³³ Gregory Tarlé,³⁴ Zhimin Zhou,²⁹ Hu Zou²⁹

¹Laboratory of Astrophysics, École Polytechnique Fédérale de Lausanne (EPFL), Observatoire de Sauverny, CH-1290 Versoix, Switzerland

²Department of Astronomy, Tsinghua University, Beijing 100084, China

³Departamento de Física Teórica, Facultad de Ciencias, Universidad Autónoma de Madrid, 28049 Madrid, Spain

⁴Centro de Investigación Avanzada en Física Fundamental (CIAFF), Facultad de Ciencias, Universidad Autónoma de Madrid, 28049 Madrid, Spain

⁵Department of Physics and Astronomy, University of Utah, Salt Lake City, UT 84112, USA

⁶IRFU, CEA, Université Paris-Saclay, F-91191 Gif-sur-Yvette, France

⁷Aix Marseille Université, CNRS, LAM (Laboratoire d'Astrophysique de Marseille) UMR 7326, F13388, Marseille, France

⁸Perimeter Institute for Theoretical Physics, 31 Caroline St. North, Waterloo, ON N2L 2Y5, Canada

⁹Waterloo Centre for Astrophysics, University of Waterloo, Waterloo, ON N2L 3G1, Canada

¹⁰Department of Physics and Astronomy, University of Waterloo, 200 University Avenue W, Waterloo, ON N2L 3G1, Canada

¹¹Center for Cosmology and AstroParticle Physics, The Ohio State University, 191 West Woodruff Avenue, Columbus, OH 43210, USA

¹²Kavli Institute for Particle Astrophysics and Cosmology, Physics Department, Stanford University, Stanford, CA 94305, USA

¹³Physics Department, Stanford University, 382 Via Pueblo Mall, Stanford, CA 94305, USA

¹⁴SLAC National Accelerator Laboratory, Menlo Park, CA 94025, USA

¹⁵Department of Physics, Kansas State University, 116 Cardwell Hall, Manhattan, KS 66506, USA

¹⁶Lawrence Berkeley National Laboratory, 1 Cyclotron Road, Berkeley, CA 94720, USA

¹⁷Physics Dept., Boston University, 590 Commonwealth Avenue, Boston, MA 02215, USA

¹⁸Department of Physics & Astronomy, University College London, Gower Street, London, WC1E 6BT, UK

¹⁹Departamento de Física, Universidad de Guanajuato—DCI, C.P. 37150, Leon, Guanajuato, México

²⁰Department of Physics, The Ohio State University, 191 West Woodruff Avenue, Columbus, OH 43210, USA

²¹Institut de Física d'Altes Energies (IFAE), The Barcelona Institute of Science and Technology, Campus UAB, E-08193 Bellaterra Barcelona, Spain

²²Departamento de Física, Universidad de los Andes, Cra. 1 No. 18A-10, Edificio Ip, CP 111711, Bogotá, Colombia

²³Department of Physics, Southern Methodist University, 3215 Daniel Avenue, Dallas, TX 75275, USA

²⁴Serra Hunter Fellow, Departament de Física, Universitat Autònoma de Barcelona, Bellaterra, Spain

²⁵Department of Astronomy, The Ohio State University, 140 W. 18th Ave., Columbus, OH 43210, USA

²⁶NSF's National Optical-Infrared Astronomy Research Laboratory, 950 N. Cherry Avenue, Tucson, AZ 85719, USA

²⁷Institució Catalana de Recerca i Estudis Avançats, Passeig de Lluís Companys, 23, E-08010 Barcelona, Spain

²⁸Department of Physics and Astronomy, Siena College, 515 Loudon Road, Loudonville, NY 12211, USA

²⁹National Astronomical Observatories, Chinese Academy of Sciences, A20 Datun Road, Chaoyang District, Beijing, 100101, People's Republic of China

³⁰Space Sciences Laboratory, University of California, Berkeley, 7 Gauss Way, Berkeley, CA 94720, USA

³¹University of California, Berkeley, 110 Sproul Hall#5800 Berkeley, CA 94720, USA

³²Department of Physics and Astronomy, Sejong University, Seoul, 143-747, Korea

³³Department of Physics & Astronomy, Ohio University, Athens, OH 45701, USA

³⁴Department of Physics, University of Michigan, Ann Arbor, MI 48109, USA

Accepted XXX. Received YYY; in original form ZZZ

ABSTRACT

We perform a SubHalo Abundance Matching (SHAM) study with two algorithms: $\{\sigma, V_{\text{ceil}}, v_{\text{smear}}\}$ -SHAM and $\{\sigma, V_{\text{ceil}}, f_{\text{sat}}\}$ -SHAM. These are designed to reproduce the clustering on 5–30 h^{-1} Mpc of DESI One Percent Survey targets: Luminous Red Galaxies (LRGs), Emission Line Galaxies (ELGs) and Quasi-Stellar Objects (QSOs) at $0.4 < z < 3.5$. These SHAM methods

★ E-mail: jiayi.yu@epfl.ch

† E-mail: czhao@tsinghua.edu.cn

are implemented on (sub)haloes from the dark-matter-only UNIT simulations. V_{ceil} is the incompleteness of the massive host (sub)haloes and is the key to the generalized SHAM. v_{smear} models the uncertainties in the spectroscopic redshift measurement. We cross-check it with results from redshift differences Δv of repeat observations, fitted well by Lorentzian profiles in general. A free satellite fraction f_{sat} is necessary to reproduce the clustering of ELGs. We find ELGs present a more complex galaxy–halo mass relation than LRGs due to their weak constraints on σ . Each tracer shows a certain range of V_{ceil} values, corresponding to the large-stellar-mass incompleteness of LRGs, the quenched star formation of ELGs and the quenched black hole accretion of QSOs. The impact of the statistical redshift uncertainty on ELG clustering is negligible. For LRGs, a Gaussian profile is a better choice for sub-samples at redshift bins. The best-fitting satellite fraction for DESI ELGs is around 4 per cent, which is lower than previous observations. The mean halo mass $\log_{10}(\langle M_{\text{vir}} \rangle)$ in $h^{-1} M_{\odot}$ for LRGs, ELGs and QSOs are 13.16 ± 0.01 , 11.90 ± 0.06 and 12.66 ± 0.45 respectively. We find the mean peak maximum circular velocity $\langle V_{\text{peak}} \rangle$ for ELGs is twice smaller than that of LRGs and QSOs. Our SHAM algorithms can also provide galaxy mocks for cosmological tests.

Key words: cosmology: large-scale structure of Universe – method: statistical – method: observational – galaxy: halo

1 INTRODUCTION

Λ CDM is the standard model of modern cosmology that describes the evolution of the Universe. In this framework, two dark components, dark matter and dark energy, comprise 95 per cent of the total energy density. The nature of dark energy can be explored using baryonic acoustic oscillation (BAO; Eisenstein & Hu 1998), a standard ruler of the universe. Meanwhile, redshift-space distortion (RSD, Kaiser 1987) embodies the growth rate of the large-scale structure (LSS) which is dominated by the evolution of dark matter.

In observation, BAO and RSD can be measured by spectroscopic galaxy surveys that observe millions of spectra of galaxies and QSOs. With BAO and RSD, the precision of cosmological parameters, such as Ω_{Λ} , H_0 and σ_8 , have reached per cent level (Alam et al. 2021b), constrained with data from the Baryon Oscillation Spectroscopic Survey (BOSS, 2008–2014; Dawson et al. 2012), and the extended BOSS (eBOSS, 2014–2020; Dawson et al. 2016) in the Sloan Sky Digital Survey¹ (SDSS; Eisenstein et al. 2011; Blanton et al. 2017). BOSS and eBOSS have probed 1,547,553 luminous red galaxies (LRGs) at $0.2 < z < 1.0$, 173,736 emission line galaxies (ELGs) at $0.6 < z < 1.1$, and 343,708 QSOs at $0.8 < z < 2.2$ (Alam et al. 2021a).

The largest ongoing spectroscopic survey, the Dark Energy Spectroscopic Instrument (DESI, 2021–2026; DESI Collaboration et al. 2016a,b) is a robotic, fiber-fed, highly multiplexed survey that operates on the Mayall 4-meter telescope at Kitt Peak National Observatory. It aims to explore the nature of dark energy via the most precise measurement of the 3D Universe in $14,000 \text{ deg}^2$ of the sky after 5 years of observations (Levi et al. 2013). The list of targets to be observed by DESI (Myers et al. 2023) is determined with the help of the imaging from the DESI Legacy Imaging Surveys (Zou et al. 2017; Dey et al. 2019; Schlegel et al. prep). The preliminary selection of targets was done in 2020 for the Milky Way Survey (MWS; Allende Prieto et al. 2020), Bright Galaxy Survey (BGS; Ruiz-Macias et al. 2020), LRG (Zhou et al. 2020), ELG (Raichoor et al. 2020), QSO (Yèche et al. 2020).

DESI started its first light observation in 2020 and will make public its Early Data Release (EDR; DESI Collaboration et al. 2023a) and the Siena Galaxy Atlas (SGA; Moustakas et al. prep) in 2023. EDR contains LSS catalogues that include redshift measurements, their corresponding random catalogues, and the clustering output (DESI Collaboration et al. 2023b; Lasker et al. prep). The One Percent Survey is a part of the EDR. It has covered around one per cent

of the 5-year sky footprint and observed more than 90,000 LRGs, 270,000 ELGs, 30,000 QSOs, and 150,000 low-redshift galaxies (Bright Galaxy Sample, BGS) (DESI Collaboration et al. 2023a). Despite the smaller numbers of galaxies and QSOs compared to the SDSS data, the number densities of tracers from the DESI One Percent Survey are larger than those of BOSS and eBOSS (introduced later in Table 2). Additionally, the rate between the observed targets and the targets of the One-Percent Surveys is larger than 85 per cent for all tracers (DESI Collaboration et al. 2023b; Lasker et al. prep). Thus, data from the One Percent Survey are sufficient for small-scale clustering analysis, such as the galaxy–halo connection study.

The relationship between haloes and galaxies is crucial for the modelling of galaxy clustering. However, this relation is highly non-linear and generally subject to local environmental effects (e.g., Tinker et al. 2011; Wetzel et al. 2012). SubHalo Abundance Matching (SHAM, Kravtsov et al. 2004; Tasitsiomi et al. 2004; Conroy et al. 2006; Behroozi et al. 2010) is an intuitive empirical method to model this non-linear relation based on N -body simulations that resolve hierarchical structures, including both haloes and subhaloes. This method assigns the most massive or brightest galaxy to centres of the most massive haloes in the case of central galaxies and subhaloes for satellite galaxies. The resulting probability of hosting a central/satellite galaxy in a halo/subhalo is a function of their (sub)halo mass, $P(M_{\text{halo}})$. The shape of this probability is related to the stellar properties determined empirically.

As clustering observations and simulations improve, more advanced versions of SHAM algorithms are developed. For instance, Tasitsiomi et al. (2004) introduced a Gaussian scattering with dispersion σ to the halo mass, to model the Gaussian residual in the galaxy–halo mass relation (e.g., Willick et al. 1997; Steinmetz & Navarro 1999). Trujillo-Gomez et al. (2011) and Reddick et al. (2013) proposed using the peak maximum circular velocity, V_{peak} , instead of the halo mass, M_{vir} , as it is closely associated with stellar mass and it is immune to the tidal stripping of subhaloes and pseudo evolution of their M_{vir} . Favole et al. (2016); Rodríguez-Torres et al. (2017) proposed a SHAM implementation that takes into account the fact that ELGs and QSOs are incomplete in the massive stellar-mass end. There are also SHAM variants that make use of secondary halo/galaxy properties (e.g., Hearin et al. 2013; Favole et al. 2022). SHAM methods can also include assembly bias and orphan galaxies (Lehmann et al. 2017; Behroozi et al. 2019; Contreras et al. 2021; DeRose et al. 2022).

In this work, we use two SHAM implementations that are essentially variants of one algorithm: $\{\sigma, V_{\text{ceil}}, v_{\text{smear}}\}$ -SHAM (v_{smear} -SHAM hereafter) and $\{\sigma, V_{\text{ceil}}, f_{\text{sat}}\}$ -SHAM (f_{sat} -SHAM hereafter). The v_{smear} -SHAM was used to study BOSS/eBOSS LRGs (Yu et al.

¹ <http://www.sdss.org/>

2022, Yu22 hereafter) and here we use it to model LRGs and QSOs. Here, we introduce the f_{sat} -SHAM to be able to correctly reproduce the clustering of DESI ELGs. The free parameters in these SHAMs model the following aspects: the scatter in the galaxy–halo mass relation, σ ; an upper limit of σ -scattered V_{peak} set by V_{ceil} (in percentage), which reduces the possibility of massive (sub)haloes hosting a given type of galaxy or QSO; the uncertainty in spectroscopic redshift determination, v_{smear} ; and the fraction of satellite galaxies, f_{sat} , which we find to be only needed for reproducing the clustering of ELGs.

This paper is arranged as follows. In Section 2 we describe the early data release of DESI, including repeat observations and statistical redshift uncertainty measurements, the UNIT N -body simulation, and the covariance matrix. The SHAM implementation and fitting are introduced in Section 3. In Section 4, we present the best-fitting results of SHAM and the interpretations of parameters for different tracers. We conclude our findings in Section 5.

This paper is one of the first series papers from the DESI galaxy–halo connection topical group. Papers released with EDR for One Percent Survey analysis that utilise ABACUSUMMIT (Maksimova et al. 2021) simulations are Yuan et al. in prep for LRG and QSO HOD, Rocher et al. in prep for ELG HOD. Prada et al. in prep is an overview for SHAM based on UCHUU (Ishiyama et al. 2021). A stellar-mass-split abundance matching applied on COSMICGROWTH (Jing 2019) is also used to study DESI LRG–ELG cross-correlations (Gao et al. in prep). Other works will be published along with later data releases.

2 DATA

2.1 DESI Early Data Release

DESI, a 5-year spectroscopic survey, started instrumental tests in 2020 to ensure the 5000 fibres controlled by the robotic positioners could work properly in the focal plane over a 3-degree field of view (DESI Collaboration et al. 2022; Silber et al. 2022; Miller et al. prep). After the commissioning, DESI conducted its Survey Validation campaign (DESI Collaboration et al. 2023a). It aims to validate the spectra reduction pipeline (Guy et al. 2023), assess the quality of data provided by REDROCK² that derives the target type and redshift from spectra (Bailey et al. prep), and optimise the target selection (Schlafly et al. prep) and fibre assignment (Raichoor et al. prep) of DESI. During the campaign, it explores target selection criteria broader than those of the 5-year main survey and observes objects typically four times longer than the main survey; in addition, to perform the visual inspection, few tiles are observed approximately 10 times longer than in the main survey (Alexander et al. 2023; Lan et al. 2023). For this reason, there are many repeat observations for each object. Later in April and May of 2021, DESI observed its One Percent Survey that covered about 1 per cent of the footprint of the 5-year main survey and used target selection criteria close to those of the main survey (Cooper et al. 2022; Hahn et al. 2022; Zhou et al. 2023; Raichoor et al. 2023; Chaussidon et al. 2022). The observation field is composed of 20 non-overlapping rosettes, each observed at least 12 times. This ensures very high fibre assignment completeness (larger than 85 per cent for ELGs and over 94 per cent for the rest of the tracers) in this region (DESI Collaboration et al. 2023a,b; Lasker et al. prep). As there are more exposures for objects that do not have a reliable redshift after the first observation, data from the One Percent Survey have a high redshift-success rate.

² <https://github.com/desihub/redrock>

Our SHAM method aims to reproduce the clustering of LRGs at $0.4 < z < 1.1$, ELGs at $0.8 < z < 1.6$, and QSOs at $0.8 < z < 3.5$ from the One Percent Survey in the range $5\text{--}30 h^{-1}$ Mpc. LRG samples are divided into three smaller redshift ranges: $0.4 < z < 0.6$, $0.6 < z < 0.8$, $0.8 < z < 1.1$. ELG samples are divided into two redshift bins: $0.8 < z < 1.1$ and $1.1 < z < 1.6$. QSOs are observed at $0.8 < z < 3.5$, and are divided into $0.8 < z < 1.1$, $1.1 < z < 1.6$, $1.6 < z < 2.1$, $2.1 < z < 3.5$.

2.1.1 Galaxy Weights

To obtain an unbiased measurement in the galaxy clustering, we employ the FKP weight w_{FKP} , the pairwise-inverse-probability (PIP) weight (Bianchi & Percival 2017), and the angular-up weight (ANG) (Percival & Bianchi 2017) for pairs of galaxies. In the calculation of the effective redshift, we use the total weight w_{tot}

$$w_{\text{tot}} = w_{\text{FKP}} w_{\text{comp}} \quad (1)$$

where w_{comp} is the fibre-assignment completeness weight provided in the LSS catalogue. We briefly describe all of them below and we refer the readers to (DESI Collaboration et al. 2023b; Lasker et al. prep) for more details.

The One Percent Survey LSS catalogues provide w_{FKP} (Feldman et al. 1994) that minimises the variance in the clustering estimator (see Section 3.1) when the observed number density of tracers varies with redshift

$$w_{\text{FKP}} = \frac{1}{1 + \bar{n}(z)P_0}, \quad (2)$$

where $\bar{n}(z)$ is the average number density at redshift z , and P_0 is the amplitude of the observed power spectrum at $k \approx 0.15 h \text{ Mpc}^{-1}$. $P_0 = 10000, 4000, 6000 h^{-3} \text{ Mpc}^3$ for LRGs, ELGs and QSOs respectively (DESI Collaboration et al. 2023b).

The PIP+ANG weighting scheme has been developed to correct the missing galaxy pairs due to fibre collision. Mohammad et al. (2020) have proved that PIP+ANG weights provide an unbiased clustering down to $0.1 h^{-1}$ Mpc. So the clustering measurement provided by the EDR has implemented this weighting scheme in addition to w_{FKP} (Section 3.1). The w_{comp} provided in the LSS catalogues is for correcting the observational incompleteness due to the fibre assignment (DESI Collaboration et al. 2023b). PIP and ANG weights, as well as w_{comp} , are all calculated with simulations of fibre assignment as described in Lasker et al. (prep).

We calculate the effective redshift of pairs of galaxies at redshifts z_i and z_j (e.g., Bautista et al. 2021), with

$$z_{\text{eff}} = \frac{\sum_{i,j} w_{\text{tot},i} w_{\text{tot},j} (z_i + z_j) / 2}{\sum_{i,j} w_{\text{tot},i} w_{\text{tot},j}}, \quad (3)$$

The effective volume $V_{\text{eff,obs}}$ (Wang et al. 2013) also involves P_0 as

$$V_{\text{eff}} = \sum_i \left(\frac{\bar{n}(z_i)P_0}{1 + \bar{n}(z_i)P_0} \right)^2 \Delta V(z_i), \quad (4)$$

where $\Delta V(z_i)$ is the comoving survey volume and $\bar{n}(z_i)$ is the mean number density of the tracer inside the redshift bin z_i . The effective number density is calculated as

$$n_{\text{eff}} = \sqrt{\frac{\sum_i \bar{n}(z_i)^2 \Delta V(z_i)}{\sum_i \Delta V(z_i)}} \quad (5)$$

We present in Table 2 all the tracers we use, their redshift ranges and the corresponding effective redshifts z_{eff} , the effective volume V_{eff} and the number density n_{eff} .

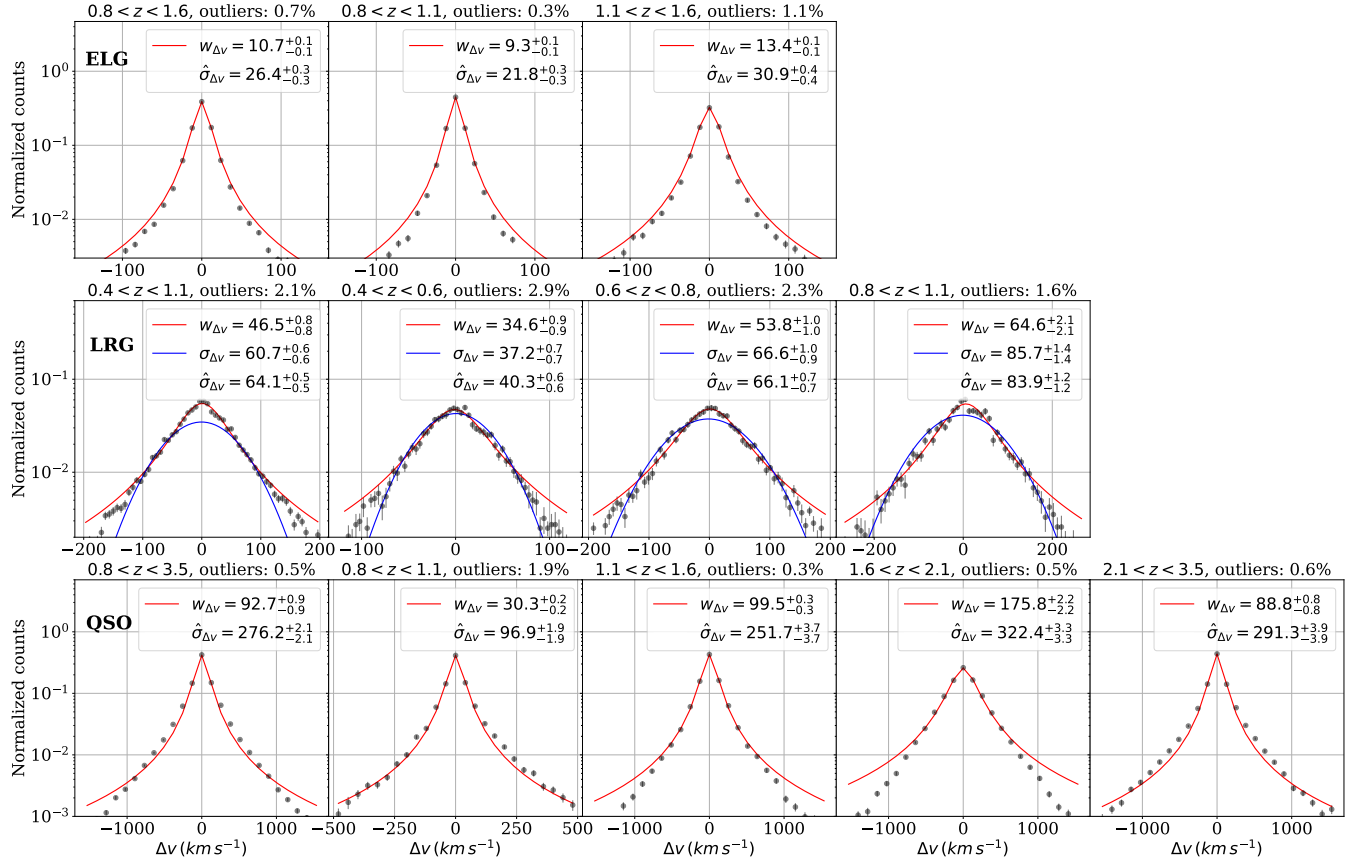


Figure 1. The statistical redshift uncertainty estimated with the histogram of the redshift difference (black filled circles with error bars) from repeat observation taken during the early stage of Survey Validation. The first, second and third rows are ELGs, LRGs and QSOs respectively. The first columns of all rows are results for total samples, while the rest are for sub-samples at redshift bins. The statistical redshift uncertainty measured by Lorentzian functions $w_{\Delta v}$ (solid red lines) and standard deviations $\hat{\sigma}_{\Delta v}$ of Δv is presented in the label of each subplot. For LRG samples, we also fit Δv histograms with Gaussian functions (blue solid lines), providing their best-fitting dispersion $\sigma_{\Delta v}$ in the label as well. The fraction of Δv that are not included in the fittings is indicated as outlier fractions in titles.

2.2 Repeat Observations and Statistical Redshift Uncertainty

The spectroscopic measurements of redshift have associated uncertainties (i.e., the redshift uncertainty) due to factors like the spectral line width, observing conditions, and different astrophysical effects. The impact of the redshift uncertainty is equivalent to adding stochasticity to the peculiar velocity of the observed object, and thus will bias the measurement of anisotropic clustering and velocity bias (Guo et al. 2015; Hou et al. 2018; Yu et al. 2022). The redshift uncertainty can be quantified by repeat observations statistically and via its influence on the clustering using our SHAM method (see Section 3.2). The results of those two estimators should be consistent.

Objects observed repetitively exist in all stages of Survey Validation. However, the ones from the One Percent Survey are biased towards faint objects by design (see Section 2.1). Therefore, we used data from the early stage of Survey Validation to obtain an unbiased estimate of the redshift uncertainty. The redshift difference, Δz , is calculated for all pairs of repeated spectra for each object and then converted to radial velocity using $\Delta v = c\Delta z/(1+z)$, where c is the speed of light and z is the mean redshift of the pairs. Δv measurements larger than the redshift failure threshold (1000 km s⁻¹ for LRGs and ELGs, 3000 km s⁻¹ for QSOs) are then removed.

The histograms of the redshift difference of ELGs, LRGs, and QSOs are presented in Fig. 1 in black dots. The error bars of

those histograms are calculated using the delete-one jackknife method. Our fitting range is around $[-200, 200]$ km s⁻¹ for LRGs, $[-150, 150]$ km s⁻¹ for ELGs, and $[-1600, 1600]$ km s⁻¹ for QSOs except for $[-500, 500]$ km s⁻¹ for QSOs at $0.8 < z < 1.1$. The title of each subplot in Fig. 1 shows the percentage of Δv measurements that are beyond the fitting range. For SDSS BOSS/eBOSS LRGs, the redshift difference in all redshift ranges can be well fitted by Gaussian functions (Ross et al. 2020; Lyke et al. 2020; Yu et al. 2022). For DESI, all tracers show a preference for Lorentzian distributions in general (solid red lines in Fig. 1) as

$$\mathcal{L}(p, w_{\Delta v}) = \frac{A}{1 + ((x-p)/w_{\Delta v})^2}. \quad (6)$$

In Eq. (6), A is a normalization factor, p is the location of the peak value on the x-axis, and $2w_{\Delta v}$ is the full-width-half-maximum of the Lorentzian distribution. In addition, we also try to describe Δv histograms of LRGs with Gaussian profiles $\mathcal{N}(\mu, \sigma_{\Delta v})$ (solid blue lines in Fig. 1). We will discuss which profile to use for SHAM in Section 4.4. As p and μ are well consistent with 0, we present the best fitting Lorentzian $w_{\Delta v}$ and Gaussian $\sigma_{\Delta v}$ on the labels of Fig. 1. We also calculate the standard deviation of the redshift difference $\hat{\sigma}_{\Delta v}$.

In Fig. 1, we observe a much smaller redshift uncertainty for the ELGs than that of the LRGs and QSOs. The maximum $w_{\Delta v}$ of ELGs

is $13.4 \pm 0.1 \text{ km s}^{-1}$, while the minimum w_{Δ_V} of LRG and QSOs is 34.6 ± 0.9 and $30.2 \pm 0.2 \text{ km s}^{-1}$ respectively. This can be attributed to the narrow [O II] emission for ELG redshift determination, compared with absorption lines of LRGs and broad emissions of QSOs. Additionally, galaxy samples (LRGs and ELGs) show increasing uncertainty with redshift. This is because galaxies are fainter at higher redshift, and spectral lines for redshift determination have a decreasing signal-to-noise ratio and larger uncertainty. But for QSO this is not the case, as QSOs at higher redshifts are not necessarily fainter. Another reason for the non-monotonic QSO w_{Δ_V} trend is that the measurement made by repeat observation is no longer reliable at $z \gtrsim 1.5$. We will explain this in detail in Section 4.4.

2.3 *N*-body Simulation: UNIT

We apply our SHAM on Universe *N*-body simulations for the Investigation of Theoretical models from galaxy surveys³ (UNIT; Chuang et al. 2019) to generate model galaxies in cubic boxes. Planck cosmology (Planck Collaboration et al. 2016) is employed in the UNIT simulations and our SHAM implementation: $\Omega_m = 0.3089$, $h \equiv H_0/100 \text{ km s}^{-1} \text{ Mpc}^{-1} = 0.6774$, $n_s = 0.9667$, $\sigma_8 = 0.8147$. In each $1 h^{-3} \text{ Gpc}^3$ UNIT simulation box, there are 4096^3 particles with the mass resolution of $1.2 \times 10^9 h^{-1} M_\odot$.

We use UNIT halo catalogues with subhaloes identified by the ROCKSTAR (Behroozi et al. 2013a) halo finder that provides properties at the current snapshot, such as positions, peculiar velocities, virial mass M_{vir} , and the maximum circular velocity V_{max} . We regard M_{vir} of haloes with more than 50 dark matter particles to be reliable, i.e., $M_{\text{vir}}^{\text{good}} > 6 \times 10^{10} h^{-1} M_\odot$. The merger/stripping histories of haloes and subhaloes are provided by CONSISTENT TREES (Behroozi et al. 2013b). They are used to determine their peak maximum circular velocity throughout the accretion history, i.e., V_{peak} , which is the proxy of halo mass in our SHAM study.

Thanks to the fixed-amplitude method (Angulo & Pontzen 2016) used by the UNIT simulations, the effective volume of a UNIT box can be as large as $10 h^{-3} \text{ Gpc}^3$ (Chuang et al. 2019). This is up to 100 times higher than the observations presented in Table 2. So we can take just one simulation box in each snapshot and ignore the influence of the UNIT cosmic variance on our SHAM fitting.

UNIT includes 128 snapshots of simulations from redshift 99 to 0 and we employ 14 of them with their redshift presented in the fourth column of Table 2. We select the UNIT snapshot whose redshift is the closest to the z_{eff} (Eq. (3)) of the corresponding DESI sample among all the snapshots.

3 METHOD

3.1 Galaxy Clustering

The two-point correlation function (2PCF) measures the excess probability of finding a galaxy pair compared to a random distribution in a given volume. For observations, we use the Landy–Szalay estimator (LS; Landy & Szalay 1993) which minimises the variances of the measurements for an irregular geometry:

$$\xi_{\text{LS}} = \frac{\text{DD} - 2\text{DR} + \text{RR}}{\text{RR}}, \quad (7)$$

where the data–data (DD), data–random (DR), and random–random (RR) pair counts are normalized by their corresponding total number

of pairs. ξ and the pair counts can be calculated as a function of the pair separation s and μ which is the cosine of the angle between the line connecting the galaxy pairs and the line-of-sight. w_{FKP} is applied to every individual galaxy in the data and random catalogue. PIP weights are applied to DD pair counts, and ANG weights are implemented to both the DD and DR pairs.

The SHAM galaxies are populated in periodic boxes based on halo catalogues from the UNIT *N*-body simulation, so we use the Peebles–Hauser estimator (PH; Peebles & Hauser 1974) to obtain their 2PCF as follows:

$$\xi_{\text{PH}} = \frac{\text{DD}}{\text{RR}} - 1, \quad (8)$$

Unlike observation that requires random catalogues to calculate RR pairs, we use the following expression to calculate them analytically in the simulation box:

$$\text{RR} = \frac{4\pi}{3} \frac{s_{\text{max}}^3 - s_{\text{min}}^3}{V_{\text{box}}} \frac{1}{N_\mu}, \quad (9)$$

where s_{max} and s_{min} are the boundaries of the separation bins, $V_{\text{box}} = 1 h^{-3} \text{ Gpc}^3$ is the volume of the UNIT simulation box, and $N_\mu = 200$ is the number of μ bins.

By weighting the 2D $\xi(s, \mu)$ with Legendre polynomials $P_\ell(\mu)$, we obtain the 1D ξ multipoles as

$$\xi_\ell(s) = \frac{2\ell + 1}{2} \int_{-1}^1 \xi(s, \mu) P_\ell(\mu) d\mu. \quad (10)$$

We fit our SHAM to observations based on the monopole and quadrupole, i.e., $\ell = 0, 2$. We use 10 logarithmic s bins in $(5, 30) h^{-1} \text{ Mpc}$ and 200 μ bins in $(-1, 1)$.

The projected 2PCF is calculated for cross-checking the clustering of the best-fitting SHAM galaxies. This is calculated as

$$w_p(r_p) = \int_{-\pi_{\text{max}}}^{\pi_{\text{max}}} \xi(r_p, \pi) d\pi, \quad (11)$$

where $\pi_{\text{max}} = 30 h^{-1} \text{ Mpc}$ to avoid the contamination of the systematics on larger scales as shown in Yu22. PYCORR and CORRFUNC Python packages (Sinha & Garrison 2019; Sinha & Garrison 2020) are used to calculate $\xi_\ell(s)$ and w_p .

In observations, 2PCFs are calculated in redshift space. So the position of our mock galaxies produced by SHAM should take into account the redshift-space distortion (RSD; Kaiser 1987) using:

$$Z_{\text{redshift}} = Z_{\text{real}} + \frac{v_{\text{pec},Z}(1+z)}{H(z)}, \quad (12)$$

where Z is the coordinate in the Z -axis which is the line of sight, and its subscripts ‘redshift’ and ‘real’ illustrate that the coordinate is in the redshift space or in the real space. $v_{\text{pec},Z}$ is the proper peculiar velocity of SHAM galaxies along the Z -axis, and z is the redshift of the simulation snapshot. As the cosmic variance of UNIT simulations is small, we can safely ignore the variations in quadrupoles for different line-of-sights (Smith et al. 2021).

3.2 SHAM Implementation

SubHalo Abundance Matching (SHAM) is an empirical method to construct a realistic, monotonic galaxy–halo mass relation based on *N*-body simulations. In its simplest form, a SHAM has a single free parameter σ relating the masses of galaxies and haloes and can successfully reproduce the observed clustering (e.g., Tasitsiomi et al. 2004; Behroozi et al. 2010). As observations provide the clustering of multiple tracers with higher and higher accuracy, this prototype

³ <http://www.unitsims.org/>

should also be improved. We thus introduce the massive (sub)halo incompleteness V_{ceil} , the redshift uncertainty v_{smear} , and a free satellite fraction f_{sat} in the SHAM implementation besides the galaxy–halo mass scatter σ .

In our study, all (sub)haloes in the simulation have their V_{peak} multiplied by an asymmetric Gaussian as

$$V_{\text{scat}} = V_{\text{peak}} \times \begin{cases} 1 + \mathcal{N}(0, \sigma), & \mathcal{N}(0, \sigma) > 0; \\ \exp(\mathcal{N}(0, \sigma)), & \mathcal{N}(0, \sigma) < 0, \end{cases} \quad (13)$$

to avoid negative V_{scat} .

Then those (sub)haloes are sorted in descending order of V_{scat} and the first $V_{\text{ceil}}N_{\text{UNIT}}/100$ ones are removed. N_{UNIT} is the total number of haloes and subhaloes in this UNIT simulation. It means the most massive (sub)haloes will not be assigned with a galaxy/QSO in its centre. V_{ceil} is introduced for target selections that possibly remove some of the most massive LRGs, resulting in incompleteness in the host (sub)halo mass. ELGs are mostly star-forming galaxies and thus are not expected to be complete in stellar mass and thus (sub)halo mass (e.g. [Gonzalez-Perez et al. 2020](#); [Hadzhiyska et al. 2021](#)). This is because the hot and dense centre of massive (sub)haloes is an environment that depletes the cold gas and thus stops star formation (e.g. [Kauffmann et al. 2004](#); [Dekel & Birnboim 2006](#); [Peng et al. 2010](#)). QSOs are bright active galactic nuclei (AGN), i.e., their super-massive black holes actively accrete cold gas via discs (e.g., [Rosario et al. 2013](#)). In the semi-analytical models (SAM), the formation of AGNs with $L_{\text{bol}} \gtrsim 10^{45.1} \text{ erg s}^{-1}$ only happens at haloes with $M_{\text{vir}} \lesssim 10^{13} h^{-1} M_{\odot}$ during starbursts ([Griffin et al. 2019](#)). [Uchiyama et al. \(2018\)](#) attribute the absence of QSOs in the overdense regions (i.e., massive haloes) at $z \sim 2-3$ to the lack of wet mergers which leads to the QSO activity. In hydrodynamical simulations, [Weinberger et al. \(2018\)](#) also find that AGNs exit their high-accretion phase (i.e., the QSO phase) in the most massive galaxy at $z \sim 2$. The absence of QSOs in those massive quenched galaxies means their absence in the most massive haloes. So LRGs, ELGs and QSOs all require the V_{ceil} truncation. We point out that the truncation implemented by V_{ceil} still allows (sub)haloes with large V_{peak} with the help of σ . v_{smear} -SHAM and f_{sat} -SHAM algorithms then deviate after this step.

For v_{smear} -SHAM, we populate a central/satellite galaxy in the centre of each halo/subhalo in the V_{ceil} -truncated catalogue from the most massive ones to the least ones until we get the expected number of SHAM galaxies

$$N_{\text{gal}} = n_{\text{eff}} V_{\text{box}}, \quad (14)$$

where $V_{\text{box}} = 1 h^{-3} \text{ Gpc}^3$ is the box size of the UNIT N -body simulation. n_{eff} is the effective number density of the observed sample obtained using Eq. (5) and the values for each galaxy sample are presented in Table 2. The proper peculiar velocity of the host (sub)haloes v_{pec}^h is also assigned to their galaxies. The velocity of the galaxy along the line of sight $v_{\text{pec},Z}^g$ is then blurred by v_{smear} to mimic the effect of the redshift uncertainty as

$$v_{\text{pec},Z}^g = v_{\text{pec},Z}^h + \begin{cases} \mathcal{N}(0, v_{\text{smear},G}), & \text{Gaussian profile;} \\ \mathcal{L}(0, v_{\text{smear},L}), & \text{truncated Lorentzian profile,} \end{cases} \quad (15)$$

where $v_{\text{pec},Z}^h$ is the component of v_{pec}^h on the Z -axis, $\mathcal{N}(0, v_{\text{smear},G})$ and $\mathcal{L}(0, v_{\text{smear},L})$ are a random number sampled by a Gaussian profile or a Lorentzian profile, respectively (as discussed in Section 2.2). As the standard Lorentzian profile is heavy-tailed and subexponential, we remove $\mathcal{L}(0, v_{\text{smear}})$ larger than 400 km s^{-1} for LRGs and 2000 km s^{-1} for QSOs. We do not use the v_{smear} parameter in f_{sat} -SHAM as explained in Section 4.4.

In f_{sat} -SHAM, we further separate haloes and subhaloes from the V_{ceil} -truncated catalogue. Only the first $f_{\text{sat}}N_{\text{gal}}/100$ subhaloes are kept as hosts of ELG satellites and the first $(1 - f_{\text{sat}})N_{\text{gal}}/100$ haloes are for central ELGs. Then we assign the centre position and the proper peculiar velocity of those selected halo/subhalo to their central/satellite galaxies.

Finally, we calculate the clustering of model galaxies in redshift space produced by v_{smear} -SHAM or f_{sat} -SHAM and compare it with observations, trying to find the best-fitting parameters. LRGs and QSOs have non-negligible redshift uncertainties, as shown in Section 2.2, so we fit their clustering with v_{smear} -SHAM. f_{sat} -SHAM is designed to fit better the 2PCF of ELGs. In Appendix A, we present the impact of σ , V_{ceil} , v_{smear} and f_{sat} on the clustering of SHAM galaxies on $5-30 h^{-1} \text{ Mpc}$, i.e., their 2PCF monopole, quadrupole and the projected 2PCF. We further discuss the performance of the complete 4-parameter SHAM $\{\sigma, V_{\text{ceil}}, v_{\text{smear}}, f_{\text{sat}}\}$ in Appendix A.

Note that in v_{smear} -SHAM, the satellite fraction f_{sat} is defined as the percentage of subhaloes in the list of (sub)haloes selected by SHAM, that is,

$$f_{\text{sat}} \equiv \frac{N_{\text{sat}}}{N_{\text{gal}}} = \frac{N_{\text{sub,SHAM}}}{N_{\text{sub,SHAM}} + N_{\text{halo,SHAM}}} \quad (16)$$

where N_{sat} is the number of satellite galaxies in the SHAM galaxy catalogue, $N_{\text{sub,SHAM}} = N_{\text{sat}}$ is the number of subhaloes selected by SHAM, and $N_{\text{halo,SHAM}}$ is the number of haloes selected by SHAM. Note that f_{sat} is different from the percentage of subhaloes in the UNIT simulations:

$$f_{\text{sub}} \equiv \frac{N_{\text{sub}}}{N_{\text{UNIT}}} = \frac{N_{\text{sub}}}{N_{\text{sub}} + N_{\text{halo}}} \quad (17)$$

where N_{sub} is the total number of subhaloes in the UNIT simulation and N_{halo} is the total number of haloes there.

3.3 SHAM Constraints

We try to find the best-fitting SHAM parameters using a Monte-Carlo sampler MULTINEST⁴ ([Feroz & Hobson 2008](#); [Feroz et al. 2009, 2019](#)) assuming a Gaussian likelihood $\mathcal{L}(\Theta)$ for our parameter constraint

$$\mathcal{L}(\Theta) \propto e^{-\frac{\chi^2(\Theta)}{2}}. \quad (18)$$

The χ^2 values are obtained as

$$\chi^2(\Theta) = (\xi_{\text{data}} - \xi_{\text{model}}(\Theta))^T \mathbf{C}^{-1} (\xi_{\text{data}} - \xi_{\text{model}}(\Theta)), \quad (19)$$

where $\Theta = \{\sigma, V_{\text{ceil}}, v_{\text{smear}}\}$ for LRG and QSO samples and $\Theta = \{\sigma, V_{\text{ceil}}, f_{\text{sat}}\}$ for ELG samples. $\xi = (\xi_0, \xi_2)$ denotes the vector composed of the 2PCF monopole and quadrupole. The subscripts ‘data’ and ‘model’ of ξ represent measurements from the observational data and SHAM mocks, respectively. \mathbf{C} is the unbiased covariance matrix that should include the variances of ξ_{data} and ξ_{model} . The variances of ξ_{model} can be further decomposed into the cosmic variance of UNIT simulation and the statistical variance due to the random processes included (Section 3.2). The variance of UNIT is considered to be negligible (Section 2.3). ξ_{model} is obtained by averaging the 2PCFs of 32 SHAM galaxy realizations generated using the same Θ with different random seeds. Because the statistical variance of 32 realizations is less than 5 per cent of the observational errors in general, increasing the number would increase the computing cost

⁴ <https://github.com/farhanferoz/MultiNest>

tracer	σ	$v_{\text{smear,L}}$ (km s^{-1})	V_{ceil} (%)	f_{sat} (%)
LRG	[0,1]	[0,200]	[0,0.15]	/
QSO	[0,2]	[0,1600]	[0,2]	/
ELG	[0,1]	/	[0,20]	[0,30]

Table 1. The priors of v_{smear} -SHAM for LRGs and QSOs, and of f_{sat} -SHAM for ELGs. Priors of v_{smear} -SHAM with a Gaussian profile $v_{\text{smear,G}}$ are the same with those with $v_{\text{smear,L}}$.

without much gain in the reliability of the parameter constraint. So \mathbf{C} can be estimated as the variance of ξ_{data} via (Hartlap et al. 2007):

$$\mathbf{C}^{-1} = \mathbf{C}_s^{-1} \frac{N_{\text{mocks}} - N_{\text{bins}} - 2}{N_{\text{mock}} - 1}, \quad (20)$$

where $N_{\text{bins}} = 20$ (Section 3.1) is the length of ξ_{data} , i.e., the total number of bins used in the SHAM fitting. \mathbf{C}_s is the jackknife covariance matrix, and is calculated using PYCORR⁵ with $N_{\text{mock}} = 128$ jackknife subsamples of the observational data. \mathbf{C}_s is thus expressed as

$$\mathbf{C}_{s,ij} = \frac{1}{N_{\text{mock}} - 1} \sum_{k=1}^{N_{\text{mock}}} [\xi_i^{(k)} - \bar{\xi}_i][\xi_j^{(k)} - \bar{\xi}_j], \quad (21)$$

where $\xi^{(k)}$ is the correlation function measured from the data with the k_{th} jackknife subsample removed, and

$$\bar{\xi}_i = \frac{1}{N_{\text{mock}}} \sum_{k=1}^{N_{\text{mock}}} \xi_i^{(k)} \quad (22)$$

is the mean 2PCF of all jackknife subsamples. The errors for the data vector are the square root of the diagonal terms of \mathbf{C} .

We employ MULTINEST, an efficient nested sampling technique, to constrain Θ . We keep the default convergence criteria which is a tolerance of 0.5 and use 200 particles for the sampling. Using a smaller tolerance or more particles takes more computing time but provides a similar posterior. The prior range for the SHAM fitting is listed in Table 1. The best-fitting parameters, which are the medians of the 16th and 84th percentiles (the $1-\sigma$ confidence limit) of the marginalized posterior distributions of individual parameters (Appendix B), their $1-\sigma$ confidence limits, and the minimum χ^2 are provided by PYMULTINEST⁶ (Buchner et al. 2014). All the derived quantities, i.e., f_{sat} (in v_{smear} -SHAM), halo occupation distribution (HOD), the probability of a (sub)halo to host a central (satellite) galaxy (PDF), the mean halo mass $\langle M_{\text{vir}} \rangle$ and the mean V_{peak} ($\langle V_{\text{peak}} \rangle$) are computed using the nested sampling chain.

4 RESULTS

We present results of v_{smear} -SHAM for LRGs and QSOs, f_{sat} -SHAM for ELGs for the DESI One Percent Survey in this section. The best-fitting 2PCF, features of the best-fitting σ , V_{ceil} , v_{smear} and f_{sat} for different tracers are discussed respectively. We also check the consistency between the HOD measured from our best-fitting SHAM with those from HOD studies using the same data.

⁵ <https://github.com/cosmodesi/pycorr>

⁶ <https://github.com/JohannesBuchner/PyMultiNest>

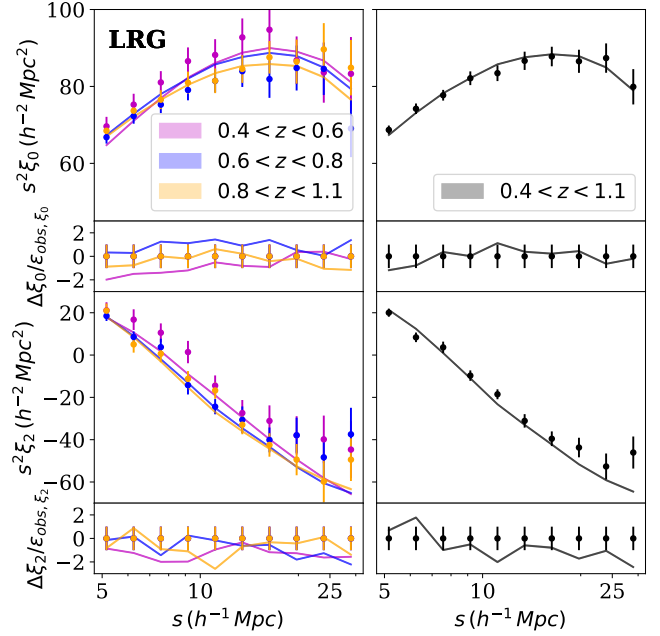


Figure 2. The clustering of observed LRGs (filled circles with error bars) compared with that of the best-fitting SHAM model galaxies with its statistical uncertainty (solid lines with shades). Monopoles and their residuals normalised by the observed errors ϵ_{obs} are presented in the first and the second rows. The third and fourth rows present those for quadrupoles. Each colour shows a different redshift range, as indicated in the legend. The first column shows results for LRGs in different redshift bins and the second for the total sample. The error bars of data are obtained from 128 jackknife samples, and the statistical uncertainty of SHAM galaxies indicated in the width of the shades is the standard deviation of its 32 realizations divided by $\sqrt{32}$. The uncertainty of best-fitting LRG SHAM galaxies is too small to be seen. Our SHAM provides good fit to the observed clustering at 5–30 h^{-1} Mpc.

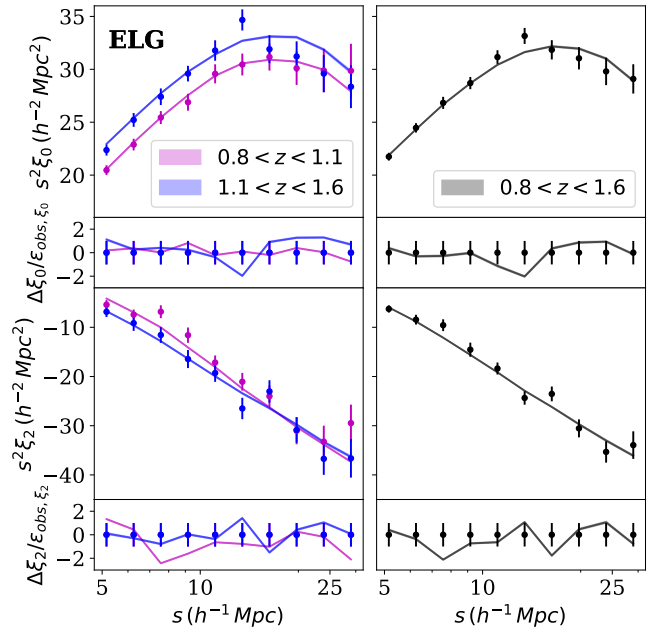


Figure 3. Same as Fig. 2 but for ELGs.

tracer type	redshift range	z_{eff}	z_{UNIT}	V_{eff} ($h^{-3} \text{Gpc}^3$)	$n_{\text{eff}} \times 10^4$ ($\text{Mpc}^{-3} h^3$)	σ	$v_{\text{smear,L}}$ (km s^{-1})	V_{ceil} (%)	f_{sat} (%)	χ^2/dof
LRG	$0.4 < z < 1.1$	0.8138	0.8188	0.150	5.50	$0.27^{+0.09}_{-0.11}$	40^{+9}_{-9}	$0.02^{+0.01}_{-0.01}$	$13.9^{+0.4}_{-0.4}$	24/17
ELG	$0.8 < z < 1.6$	1.2020	1.2200	0.204	7.26	$0.28^{+0.24}_{-0.18}$	/	$3.62^{+0.88}_{-1.10}$	$3.4^{+1.9}_{-1.6}$	22/17
QSO	$0.8 < z < 3.5$	1.7408	1.7710	0.024	0.24	$0.38^{+0.31}_{-0.24}$	215^{+24}_{-31}	$0.23^{+0.11}_{-0.09}$	$12.3^{+0.5}_{-0.5}$	9/17
LRG	$0.4 < z < 0.6$	0.5126	0.5232	0.032	6.16	$0.16^{+0.16}_{-0.11}$	27^{+17}_{-15}	$0.04^{+0.02}_{-0.02}$	$15.2^{+0.5}_{-0.5}$	15/17
LRG	$0.6 < z < 0.8$	0.7067	0.7018	0.052	6.87	$0.25^{+0.07}_{-0.10}$	19^{+12}_{-9}	$0.01^{+0.01}_{-0.01}$	$14.5^{+0.4}_{-0.4}$	23/17
LRG	$0.8 < z < 1.1$	0.9423	0.9436	0.076	4.36	$0.28^{+0.15}_{-0.14}$	30^{+14}_{-12}	$0.04^{+0.03}_{-0.02}$	$13.2^{+0.5}_{-0.5}$	29/17
ELG	$0.8 < z < 1.1$	0.9565	0.9436	0.088	10.47	$0.31^{+0.43}_{-0.21}$	/	$6.68^{+2.17}_{-2.69}$	$5.5^{+2.5}_{-2.2}$	18/17
ELG	$1.1 < z < 1.6$	1.3397	1.3210	0.121	5.13	$0.27^{+0.31}_{-0.17}$	/	$3.07^{+0.80}_{-1.09}$	$4.2^{+2.4}_{-2.1}$	22/17
QSO	$0.8 < z < 1.1$	0.9658	0.9436	0.003	0.29	$0.52^{+0.49}_{-0.30}$	101^{+87}_{-59}	$0.67^{+0.52}_{-0.23}$	$20.1^{+1.2}_{-1.2}$	17/17
QSO	$1.1 < z < 1.6$	1.3665	1.3720	0.009	0.36	$0.32^{+0.49}_{-0.21}$	78^{+35}_{-26}	$0.45^{+0.21}_{-0.21}$	$15.9^{+0.8}_{-0.8}$	11/17
QSO	$1.6 < z < 2.1$	1.8320	1.8330	0.008	0.31	$0.25^{+0.44}_{-0.18}$	273^{+151}_{-61}	$0.26^{+0.09}_{-0.15}$	$11.5^{+0.8}_{-0.8}$	13/17
QSO	$2.1 < z < 3.5$	2.4561	2.4580	0.004	0.13	$0.29^{+0.45}_{-0.18}$	542^{+75}_{-100}	$0.14^{+0.07}_{-0.09}$	$8.1^{+0.7}_{-0.7}$	12/17

Table 2. The information for observation and its best-fitting SHAM results of v_{smear} -SHAM with Lorentzian redshift uncertainty profile $v_{\text{smear,L}}$ and f_{sat} -SHAM. The columns are: 1) observed tracer type, 2) redshift range, 3) effective redshift calculated using Eq. (3), 4) redshift of the UNIT simulation snapshot for the SHAM fitting that is close to z_{eff} , 5) the effective volume V_{eff} of the observed tracer at the corresponding redshift range obtained with Eq. (4), 6) the effective number density n_{eff} calculated with Eq. (5) multiplied by 10^4 , the best-fitting parameters, i.e., 7) σ , 8) the redshift uncertainty $v_{\text{smear,L}}$, 9) the massive-(sub)halo incompleteness V_{ceil} , 10) the satellite fraction f_{sat} and 11) the minimum χ^2 divided by the degree of freedom. v_{smear} of ELG samples are asserted to 0 and the satellite fraction of LRGs and QSOs is a derived parameter from the nested sampling chain.

redshift range	σ	$v_{\text{smear,G}}$ (km s^{-1})	V_{ceil} (%)	f_{sat} (%)	χ^2/dof
$0.4 < z < 1.1$	$0.21^{+0.14}_{-0.10}$	95^{+12}_{-14}	$0.03^{+0.02}_{-0.02}$	$14.7^{+0.3}_{-0.3}$	24/17
$0.4 < z < 0.6$	$0.14^{+0.11}_{-0.08}$	67^{+28}_{-30}	$0.04^{+0.02}_{-0.02}$	$15.2^{+0.4}_{-0.4}$	15/17
$0.6 < z < 0.8$	$0.31^{+0.04}_{-0.06}$	42^{+16}_{-22}	$0.00^{+0.01}_{-0.00}$	$14.7^{+0.3}_{-0.3}$	23/17
$0.8 < z < 1.1$	$0.28^{+0.19}_{-0.17}$	84^{+17}_{-18}	$0.04^{+0.03}_{-0.03}$	$14.7^{+0.3}_{-0.3}$	30/17

Table 3. The best-fitting results of the v_{smear} -SHAM fitting for LRGs with Gaussian $v_{\text{smear,G}}$.

4.1 Clustering

We fit the 2PCF multipoles of the LRG, ELG and QSO samples from the DESI One Percent Survey at scales of $5\text{--}30 h^{-1} \text{Mpc}$ over the redshift range $0.4 < z < 3.5$ with our SHAM algorithms. Table 2 summarises the best-fitting parameters and their corresponding $1\text{-}\sigma$ confidence intervals, as well as the minimum χ^2 divided by the number of degrees of freedom. Note that v_{smear} -SHAM results presented in Table 2, Figures 2–4 and in the appendices all use a Lorentzian $v_{\text{smear,L}}$. In this case, f_{sat} is obtained as a derived parameter from the Monte-Carlo chain.

Figures 2–4 are the 2PCF monopole (first row) and quadrupole (third row) of the observed tracers (filled circles with error bars) and model galaxies/QSOs generated using SHAM with the minimum- χ^2 parameter set (solid lines). The shaded area around the SHAM clustering is the standard deviation of 2PCFs for all 32 SHAM realizations divided by $\sqrt{32}$. The observed error-rescaled residuals are presented in the second (monopole) and fourth (quadrupole) rows.

The observed clustering of LRG samples is well-fitted by v_{smear} -SHAM as shown in Fig. 2. The reduced χ^2 value of LRG fitting at

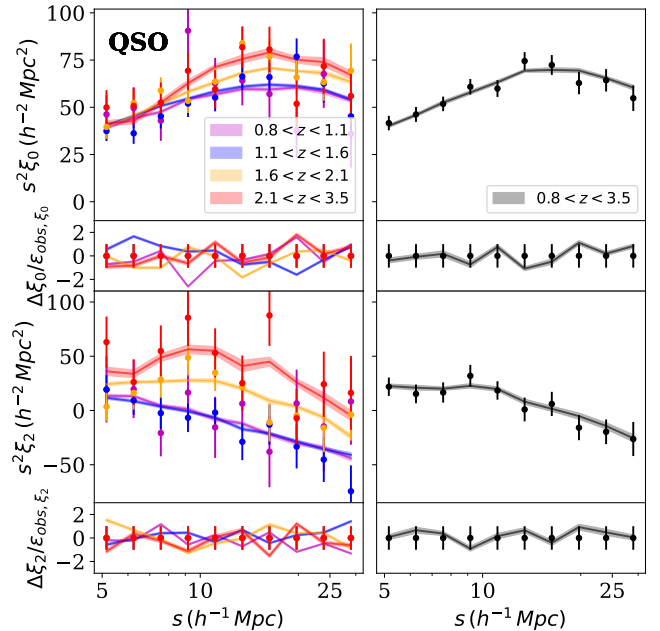


Figure 4. Same as Fig. 2 but for QSOs.

$0.8 < z < 1.1$ is around 1.7, which could be explained by underfitting. But SHAM LRGs at $0.8 < z < 1.1$ also reproduced w_p at $5 < r_p < 30 h^{-1} \text{Mpc}$ (see Appendix C for the consistent projected 2PCF of SHAM LRGs and observations at this redshift bin). So we attribute this large value to the off-diagonal terms in its jackknife covariance

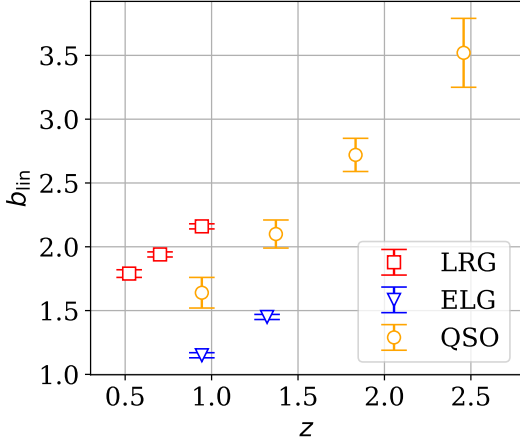


Figure 5. The linear bias of the best-fitting model galaxies and quasars from SHAM with error bars. They are calculated via the power spectrum at $k < 0.05 h \text{ Mpc}^{-1}$. For each type of tracer, the linear bias increases with the redshift.

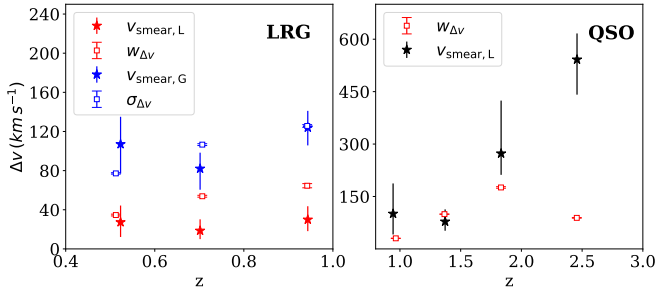


Figure 6. The redshift uncertainty quantified by the best-fitting SHAM v_{smear} (filled stars with error bars, the subscripts ‘L’ and ‘G’ stand for Lorentzian and Gaussian profiles) and that estimated statistically by the repeat observation Δv (empty squares with error bars, $w_{\Delta v}$ for Lorentzian and $\sigma_{\Delta v}$ for Gaussian) for galaxies in different redshift slices. The results of Lorentzian profiles are in red colours and those of Gaussian profiles are in blue. For DESI LRGs, SHAM $v_{\text{smear,L}}$ are systematically lower than $w_{\Delta v}$. In the case of the Gaussian profile, the SHAM $v_{\text{smear,G}}$ and $\sigma_{\Delta v}$ (both with vertical offsets) agree with each other. For QSOs, the statistical uncertainty $w_{\Delta v}$ is not consistent with the SHAM $v_{\text{smear,L}}$ (black filled stars with error bars) at $z > 1.5$.

matrix. All SHAM LRGs at $0.4 < z < 0.8$ have underestimated ξ_2 at $r > 20 h^{-1} \text{ Mpc}$, where observations present a plateau while the quadrupole of SHAM decreases. This may be attributed to some uncorrected systematics. But the underestimation may also indicate some shortcomings in our current understanding of the relationship between (sub)haloes and LRGs as was found in many BOSS and eBOSS galaxy mocks (e.g., Kitaura et al. 2016; Rodríguez-Torres et al. 2016; Zhao et al. 2021; Yu et al. 2022), especially on red galaxies (Ross et al. 2014). A detailed investigation of this problem is left for future work.

ELG multipoles are well reproduced by SHAM galaxies at all redshift ranges as shown in Fig. 3 and indicated by the reduced χ^2 values in Table 2. QSO clustering has large observed errors due to the small number density of QSOs, which leads to large shot noise. Fig. 4 proves that v_{smear} -SHAM provides a consistently good description of the observation of QSOs in a large redshift range from $z = 0.8$ to $z = 3.5$.

With the best-fitting catalogues of SHAM galaxies/quasars, we

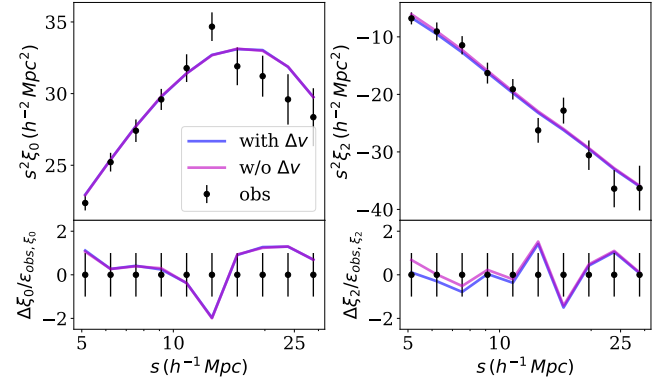


Figure 7. The effect of the maximum ELG redshift uncertainty $w_{\Delta v} = 13.4 \text{ km s}^{-1}$ on the 2PCF monopole (left) and quadrupole (right). Multipoles of SHAM galaxies without $v_{\text{smear,L}}$ are in magenta lines, the ones with $v_{\text{smear,L}} = 13.4 \text{ km s}^{-1}$ are in blue lines. Data are plotted in filled circles with error bars and the residuals normalized by the observed error bars are presented in the second row. No significant clustering effect is induced by the largest redshift uncertainty of ELGs at $5\text{--}30 h^{-1} \text{ Mpc}$.

calculate their power spectrum with `PYPOWSPEC`⁷ for the linear bias b_{lin} via

$$b_{\text{lin}}(z) = \left\langle \left(\frac{P_g(k, z)}{P_m^{\text{lin}}(k, z=0)} \right)^{\frac{1}{2}} \frac{1}{D(z)} \right\rangle_{k < 0.05 h \text{ Mpc}^{-1}} \quad (23)$$

where $P_g(k, z)$ is the power spectrum of SHAM galaxies at redshift z , $P_m^{\text{lin}}(k, z=0)$ is the linear matter power spectrum used by UNIT simulations renormalized to $z = 0$. Both power spectra are in real space. $D(z)$ is the linear growth rate at redshift z . $k < 0.05 h \text{ Mpc}^{-1}$ in Eq. (23) means that the result is obtained by averaging over this k range.

Fig. 5 presents b_{lin} of LRGs (red), ELGs (blue) and QSOs (yellow) at different redshifts. The error bars are the weighted standard deviation of the linear bias for SHAM galaxies in the Monte-Carlo chain. b_{lin} increases with the redshift for each tracer. Studies using the same DESI EDR data show the same trend Rocher et al. in prep and Prada et al. in prep. This is partly due to the fact that we can observe more faint objects at low redshift than at higher redshift. So the observed galaxies/quasars at a low redshift do not only trace the most overdense regions of dark matter, but also regions with less excess matter. Thus they present lower b_{lin} than those at a high redshift.

4.2 Scatter σ in galaxy–halo mass relation

As discussed in Yu22, σ in our v_{smear} -SHAM is composed of the intrinsic scatter in the galaxy–halo mass relation and the completeness for galaxies with an intermediate stellar mass. For LRG samples, $\sigma \sim 0.2$ dex. However, since there is a degeneracy between σ and V_{ceil} (see Appendix B for the posteriors of LRGs), it is not clear whether there is a redshift evolution in σ . For ELG samples, the constraints in σ are weak regardless of the prior range. Given its large number density, this is not the result of large errors in clustering, as is the case for QSOs. The (sub)halo incompleteness of ELGs is related to their incompleteness in stellar mass and in luminosity (Favole et al. 2016; Gonzalez-Perez et al. 2020). This leads to a complex galaxy property–halo mass connection for ELGs, thus a weakly constrained

⁷ <https://github.com/dforero0896/pypowspec>

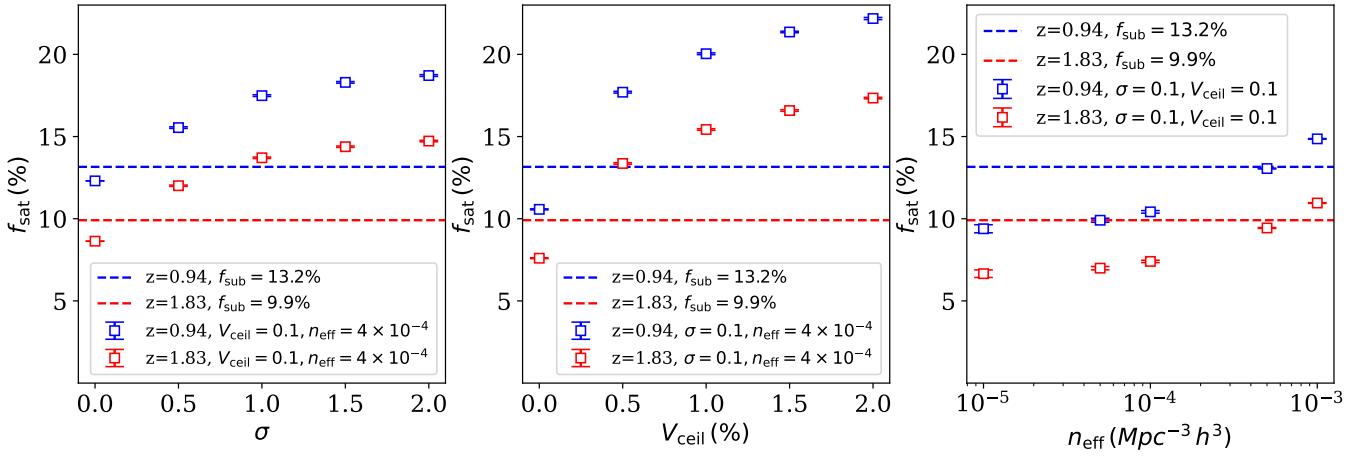


Figure 8. f_{sat} evolution with σ (left panel), V_{ceil} (middle panel) and n_{eff} (right panel) for model galaxies of SHAM at $z = 0.94$ (red empty error bars) and those at $z = 1.83$ (blue empty error bars) produced by v_{smear} -SHAM. We present the dependence of f_{sat} with one parameter and fix the other two parameters (typical values for LRGs) as indicated in the label. The error bar of f_{sat} is the standard deviation of f_{sat} among 32 realizations. The subhalo fraction of the UNIT simulation at $z = 0.94$ (red) and $z = 1.83$ (blue) defined in Eq. (17) is plotted in dashed lines.

σ as it integrates many factors. σ also leads to the stochastic variance in the clustering of SHAM galaxies. For the LRG and ELG samples, this variance is as small as 5 per cent of the observational error ϵ_{obs} (not visible as shown in Fig. 2–3). So we can also ignore its effect on the final χ^2 values in general.

4.3 Massive (Sub)Halo Incompleteness V_{ceil}

For LRGs, V_{ceil} describes the halo/stellar mass incompleteness at the massive end. As shown in LRG posteriors (See Appendix B), V_{ceil} values for LRGs are very small but are definitely non-zero at $1-\sigma$ level. This incompleteness can be attributed to the fact that the target selection of LRGs removes some of the most massive blue galaxies, leading to empty massive haloes. It also results in a decreasing halo occupation of central galaxies as presented in Section 4.6.

For ELG samples, V_{ceil} is critical to describe their absence in the centre of massive (sub)haloes. ELG entries in Table 2 show that we shall remove a per-cent level of (sub)haloes, allowing few (sub)haloes with $V_{\text{peak}} > 300 \text{ km s}^{-1}$ to host an ELG at their centre (Fig. 12). Since there is no degeneracy among parameters of the f_{sat} -SHAM, the $1 - \sigma$ difference between the V_{ceil} of ELGs at $0.8 < z < 1.1$ and $1.1 < z < 1.6$ embodies their clustering difference.

QSOs at $0.8 < z < 1.1$ show a larger V_{ceil} than that of QSOs at higher redshifts, but this difference is not significant due to the weak constraint. This is consistent with Chaussidon et al. (2022) in which QSOs at $z < 1.0$ show a smaller purity than those at high redshifts. Even though V_{ceil} for QSOs only exclude less than 1 per cent of (sub)haloes with the largest V_{scat} (Eq. (13)), the clustering of QSOs cannot be well-fitted without the V_{ceil} parameter. As explained in Section 3.2, this is consistent with findings of SAM studies (e.g., Griffin et al. 2019) and observations (e.g., Uchiyama et al. 2018), in which QSOs are absent in the centre of the most massive (sub)haloes.

4.4 Redshift Uncertainty v_{smear}

v_{smear} -SHAM uses a Lorentzian $v_{\text{smear,L}}$ by default as this is a good model for DESI tracers in general. In particular, for LRGs, Lorentzian and Gaussian profiles can both describe the redshift difference distribution of LRG repeat observations (Fig. 1). So we perform v_{smear} -

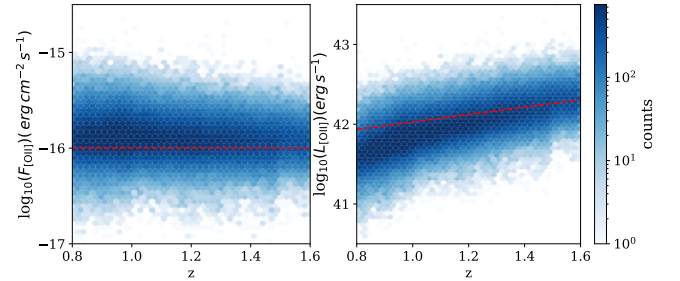


Figure 9. The flux (in $\text{erg cm}^{-2} \text{ s}^{-1}$) and the luminosity (in erg s^{-1}) of [O II] emission for ELGs as a function of the redshift. The red lines are the strong [O II] emitter threshold. The line on the left represents the standard of Gonzalez-Perez et al. (2018) with $F_{[\text{O II}]} > 10^{-16} \text{ erg s}^{-1} \text{ cm}^{-2}$. The one on the right shows an evolving $L_{[\text{O II}]}$ (Eq. (24)) derived from Gao et al. (2022). 71 per cent of DESI ELGs pass the $F_{[\text{O II}]}$ selection, 24 per cent pass the $L_{[\text{O II}]}$ selection.

SHAM fitting with Gaussian $v_{\text{smear,G}}$ as well and Table 3 includes the best-fitting results. The χ^2 values of SHAM with $v_{\text{smear,G}}$ are similar to those of SHAM with $v_{\text{smear,L}}$. Their best-fitting σ and V_{ceil} are also consistent with each other, meaning that the clustering effect of a truncated Lorentzian $v_{\text{smear,L}}$ and a Gaussian $v_{\text{smear,G}}$ is almost equivalent. So we need to check the v_{smear} consistency with the statistical redshift uncertainty estimated from repeat observations.

Fig. 6 is the comparison between the best-fitting SHAM v_{smear} (filled stars with error bars) and the best-fitting redshift uncertainty measured from repeat observations (empty squares with error bars) for DESI LRGs (left panel) and QSOs (right panel). The results of Lorentzian profiles are in red and those of Gaussian profiles are in blue. In particular, Gaussian profiles for LRGs are vertically shifted. The best-fitting LRG SHAM $v_{\text{smear,G}}$ values agree with the Gaussian dispersion $\sigma_{\Delta v}$ of repeat observations, while SHAM $v_{\text{smear,L}}$ values underestimate the statistical redshift uncertainty evaluated using the width of Lorentzian functions $w_{\Delta v}$. Note that the standard deviation $\hat{\sigma}_{\Delta v}$ of LRG repeats are also consistent with the dispersion of the Gaussian profile. Therefore, the Gaussian profile $v_{\text{smear,G}}$ is more

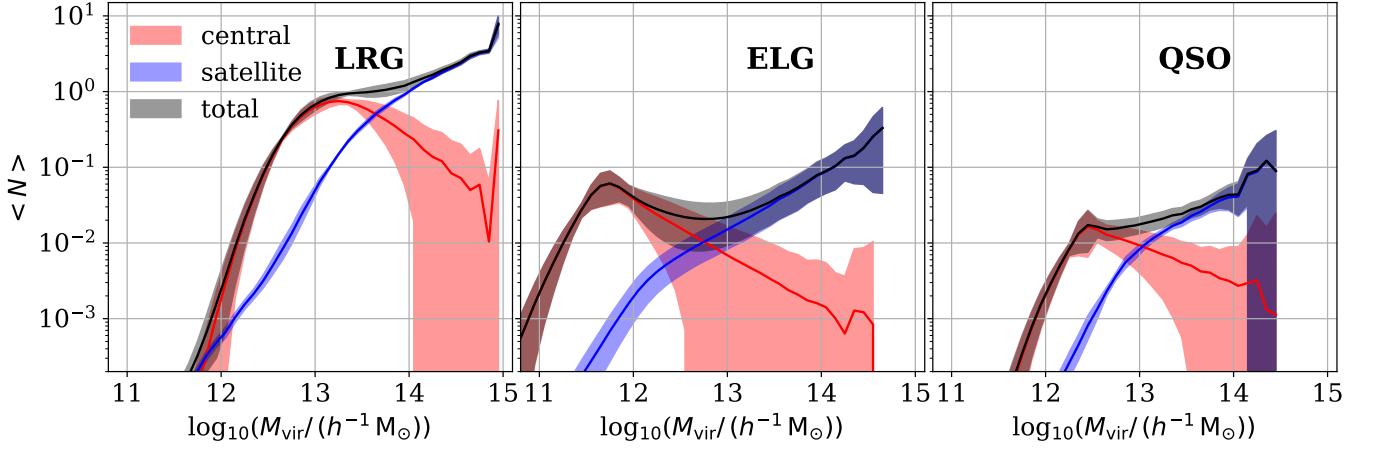


Figure 10. The average HOD of SHAM LRGs at $0.4 < z < 1.1$ (left panel), ELGs at $0.8 < z < 1.6$ (middle panel) and QSOs at $0.8 < z < 3.5$ (right panel). The contribution of central galaxies to the average HOD is shown by red lines and that of satellites by blue lines. The $1\text{-}\sigma$ errors derived from the Monte-Carlo chain are shown as shaded regions of the same colour.

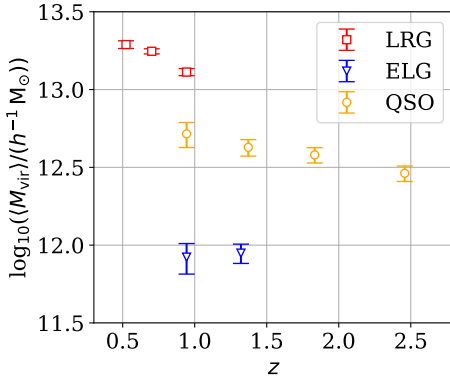


Figure 11. The evolution of the mean parent halo mass $\langle M_{\text{vir}} \rangle$ of SHAM LRGs with Gaussian $v_{\text{smear,G}}$ (red empty square with error bars), ELGs (blue empty triangle with error bars) and QSOs (orange empty circle with error bars) obtained for sub-samples at redshift slices as a function of redshift. There are three ranges of mean mass and the values of LRGs and QSOs decrease with redshift.

suitable for illustrating the uncertainty of the redshift of LRGs in redshift bins.

In contrast, the Lorentzian profile results ($w_{\Delta v} = 46.5 \pm 0.8 \text{ km s}^{-1}$ while $v_{\text{smear,L}} = 40 \pm 9 \text{ km s}^{-1}$) are in better agreement for LRGs in the full redshift range, indicating that there are multiple types of LRGs with different redshift uncertainty properties. As a result, Raichoor et al. (2023); Chaussidon et al. (2022) use a linear combination of Gaussian profiles to fit the redshift difference Δv . Nevertheless, a truncated Lorentzian with just one parameter works in the same way as multiple-Gaussian profiles in terms of the clustering effects and SHAM results.

For QSOs in the right panel of Fig. 6, SHAM $v_{\text{smear,L}}$ shows a non-decreasing trend. This reflects the quadrupole amplitude of QSOs at different redshift bins shown in the third row of Fig. 4. However, this trend is inconsistent with that of repeat observations (red empty error bars), and SHAM $v_{\text{smear,L}}$ starts to deviate from $w_{\Delta v}$ of repeat observations at $z \geq 1.5$. The discrepancy is possibly due to the switch of the main spectral line for redshift determination from Mg II and C IV (Zarrouk et al. 2018). QSO spectral lines are

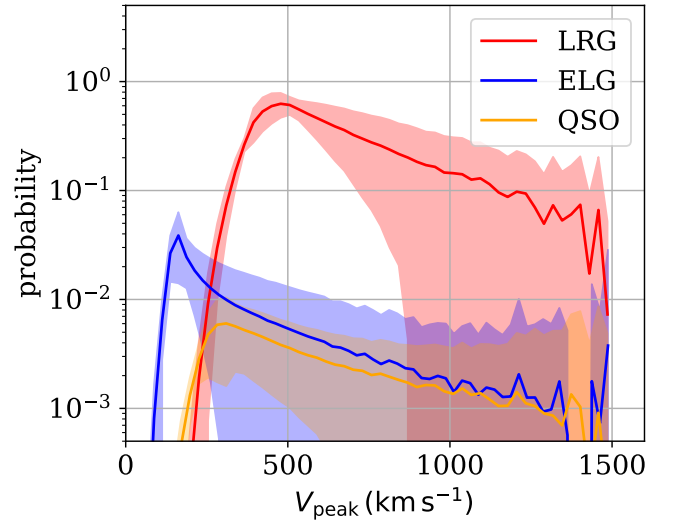


Figure 12. The probability of a (sub)halo to host an LRG (red), an ELG (blue) or a QSO (orange) as a function of V_{peak} of (sub)haloes for LRGs with Gaussian $v_{\text{smear,G}}$, ELGs and QSOs at $0.8 < z < 1.1$. The shades are their $1\text{-}\sigma$ errors calculated using the Monte-Carlo chain.

subject to systematical velocity shifts caused by astrophysical effects (e.g., Gaskell 1982; Richards et al. 2002, 2011) and repeat observations for the same object cannot capture this shift. But this shift is different from object to object, creating an extra relative random motion between QSO pairs. Moreover, Shen et al. (2016) have proved that Mg II is the least shifted broad emission of QSOs, while C IV can be strongly shifted. This will result in a larger random motion between QSO pairs at $z > 1.5$ than those at $z < 1.5$. This motion is integrated into $v_{\text{smear,L}}$ of SHAM, resulting in its fast rise at $z > 1.5$ and explaining the inconsistency between $v_{\text{smear,L}}$ and $w_{\Delta v}$.

The redshift uncertainty of ELGs is small in general as presented in Fig. 1. Its largest redshift uncertainty among ELGs samples, i.e., $v_{\text{smear,L}} = 13.4 \text{ km s}^{-1}$ for ELGs at $1.1 < z < 1.6$, does not produce a significant clustering effect, as illustrated in Fig. 7. The magenta line is the clustering of SHAM galaxies created using the

best-fitting f_{sat} -SHAM. The blue line shows the clustering with $v_{\text{smear,L}} = 13.4 \text{ km s}^{-1}$ applied to the peculiar velocity of the SHAM ELGs. For the monopole, $v_{\text{smear,L}}$ have little influence as expected, and the influence on the quadrupole is restricted to $5\text{--}8 h^{-1} \text{ Mpc}$ and is within $1\text{-}\sigma$ range of the observed jackknife error bars. Therefore, asserting $v_{\text{smear}} = 0$ for f_{sat} -SHAM does not bias the best-fitting results of the other three parameters.

4.5 Satellite Fraction f_{sat}

The fraction of satellites, f_{sat} , for LRGs and QSOs, is calculated when σ and V_{ceil} are given to v_{smear} -SHAM. We present in Fig. 8 the impact of σ , V_{ceil} and the number density n_{eff} on f_{sat} for SHAM galaxies produced by v_{smear} -SHAM at $z = 0.94$ (blue) and $z = 1.83$ (red). We f_{sub} of UNIT simulations at those redshifts are plotted in dashed horizontal lines, obtained using Eq. (17). The fixed parameters⁸ are $\sigma = 0.1$, $V_{\text{ceil}} = 0.1$, $n_{\text{eff}} = 4 \times 10^{-4} \text{ Mpc}^{-3} h^3$. f_{sat} monotonically increases with σ , V_{ceil} and n_{eff} . This is because larger σ , V_{ceil} and n_{eff} all mean selecting more (sub)haloes with small V_{peak} , corresponding to a larger fraction of subhaloes/satellites. In contrast, for σ , $V_{\text{ceil}} \sim 0$, there are a few selected subhaloes that have a large V_{peak} , resulting in $f_{\text{sat}} < f_{\text{sub}}$. Due to the tight constraints on LRG σ and V_{ceil} , the $1\text{-}\sigma$ confidence interval of LRG f_{sat} , which is a derived parameter, is also small. From another aspect, the slope of the $f_{\text{sat}}\text{--}\sigma$ and $f_{\text{sat}}\text{--}V_{\text{ceil}}$ relations decreases as σ and V_{ceil} become larger. Additionally, the slope of the $f_{\text{sat}}\text{--}n_{\text{eff}}$ relation increases with n_{eff} . The combination of these effects results in the small errors of QSO f_{sat} despite its loose constraints on σ and V_{ceil} .

The satellite fraction of v_{smear} -SHAM is also affected by the redshift, i.e., the substructure growth. f_{sat} of SHAM galaxies at $z = 1.83$ are lower than those at $z = 0.94$, calculated with the same v_{smear} -SHAM parameters. This is consistent with the decreasing trend of f_{sat} for LRGs and QSOs with the redshift.

For ELGs, we find that about 4 per cent of them are satellite galaxies when we fit the data with our f_{sat} -SHAM method. Such a low fraction of satellites is also found in models mimicking a DESI-like survey (Gonzalez-Perez et al. 2018). In the literature, for different selections of ELGs, this fraction has been found to range from $f_{\text{sat}} \sim 5$ to ~ 22.5 per cent (Favole et al. 2016; Gao et al. 2022) in VIPERS and from ~ 17 per cent (Guo et al. 2019) to 19.3 per cent (Lin et al. 2023) in eBOSS. The difference in the strength of the [O II] emission can also alter f_{sat} . For example, Gonzalez-Perez et al. (2018); Gao et al. (2022) find that strong [O II] emitters tend to have a low f_{sat} down to per cent level, i.e., 4.6 and 7.0 ± 2.0 per cent respectively. In Fig. 9 we show the distribution of DESI ELG [O II] fluxes, $F_{[\text{O II}]}$, and luminosities, $L_{[\text{O II}]}$, as a function of redshift. We find that more than 71 per cent of DESI ELGs from the One Percent Survey have $F_{[\text{O II}]} > 10^{-16} \text{ erg s}^{-1} \text{ cm}^{-2}$ (the red line on the left panel), which is the cut assumed in the theoretical study of Gonzalez-Perez et al. (2018). On the right panel, 24 per cent of them are strong [O II] emitters according to the definition in Gao et al. (2022), i.e., they should have $L_{[\text{O II}]}$ larger than

$$\log_{10} L_{[\text{O II}]}^{\text{thres}}(z) = \log_{10} L_{[\text{O II}]}^{\text{thres}}(z = 0.5) + \log_{10} \left(\frac{1+z}{1+0.5} \right)^{\beta_L} \quad (24)$$

where $z \in (0.8, 1.6)$, and $L_{[\text{O II}]}^{\text{thres}}(z = 0.5) = 10^{41.75} \text{ erg s}^{-1}$, which is the $L_{[\text{O II}]}$ lower bound of VIPERS ELGs with $f_{\text{sat}} = 7.0 \pm 2.0$ per

⁸ These are typical values for LRGs. We have checked the f_{sat} relations with typical values for QSOs and found the same trends as in Fig. 8.

cent. This fraction for VIPERS and eBOSS are 10 and 12 per cent respectively. Thus, it is reasonable if we obtain a smaller f_{sat} from the DESI data, compared to that of the eBOSS ELGs and VIPERS samples.

However, it is still possible that our satellite fraction is underestimated as we do not include orphan galaxies that are necessary for correcting the deficits of the current subhalo tracking method (Behroozi et al. 2019). We check in Appendix D the consistency between the f_{sat} measured by f_{sat} -SHAM and galaxy mocks provided by UniverseMachine (Behroozi et al. 2019) and SAM models (Gonzalez-Perez et al. 2018). The mass resolution of the UNIT simulation may also not be good enough to resolve all substructures for ELGs. Moreover, f_{sat} is model dependent (e.g., Favole et al. 2016; Gao et al. 2022). In studies for DESI ELGs, Gao et al. in prep presents a redshift- and stellar-mass-dependent satellite fraction with reconstructed orphan galaxies. Rocher et al. in prep finds that adding conformity can lead to a smaller f_{sat} compared to HOD without that. So it is difficult to compare fairly the f_{sat} value provided by different models for different galaxy surveys. We will leave those for future work.

4.6 Average Halo Occupation Distribution

Fig. 10 shows the average halo occupation distribution (HOD) of SHAM LRGs with Lorentzian $v_{\text{smear,L}}$ at $0.4 < z < 1.1$, SHAM ELGs at $0.8 < z < 1.6$ and SHAM QSOs at $0.8 < z < 3.5$ as a function of the halo mass M_{vir} . They are computed with the weights from the Monte-Carlo chain. M_{vir} corresponds to the virial mass of host haloes or parent haloes of subhaloes. For LRGs, their stellar mass is closely related to the halo mass (e.g., Leauthaud et al. 2012; Behroozi et al. 2019). Their HOD can be modelled using a 5-parameter form, with a smoothed step function for central galaxies, and a power law for satellites (e.g., Zheng et al. 2005; Zhai et al. 2017). The HOD of our central SHAM LRGs reaches $\langle N \rangle = 0.75 \pm 0.07$ at $M_{\text{vir}} = 10^{13.3} h^{-1} M_{\odot}$ and decreases towards the massive end as we set V_{ceil} free. This incompleteness is consistent with the measurement of ABACUSUMMIT HOD (Yuan et al. in prep) for DESI LRGs.

There are various HOD models for central ELG. Avila et al. 2020; Rocher et al. in prep discuss several ELG central profiles: the modified high-mass-quenched model (Alam et al. 2020), the Gaussian function, the star-forming HOD model (Avila et al. 2020), the lognormal HOD model (Rocher et al. in prep). The central HOD of our SHAM ELGs shows a preference for a star-forming HOD profile with a turning point at $M_{\text{vir}} = 10^{11.7} h^{-1} M_{\odot}$ that reaches $\langle N \rangle = 0.06 \pm 0.03$. ELGs residing in $M_{\text{vir}} > 10^{12.5} h^{-1} M_{\odot}$ are also found in the study of Gao et al. in prep.

There are also multiple profiles for QSO HOD models (Smith et al. 2020; Yuan et al. in prep). Our central QSO HOD reaches the maximum value $\langle N \rangle = 0.016 \pm 0.001$ after $M_{\text{vir}} = 10^{12.4} h^{-1} M_{\odot}$. Note that no tracer reaches $\langle N \rangle = 1$. It means that we will not find one galaxy/QSO in every halo above a certain halo mass. It is consistent with the V_{ceil} results that LRGs from the One-Percent Survey are not complete, while ELGs and QSOs are absent from massive haloes due to physical reasons.

Note that the decreasing number of central galaxies/quasars in the massive halo in Fig. 10 (red lines with shades) occurs because we apply a simple truncation to the massive haloes via V_{ceil} . This halo-mass incompleteness can be introduced with other implementations like LRG/QSO HOD in Yuan et al. in prep that results in a flat central HOD shape or ELG HOD with four formats of decreasing trends in Rocher et al. in prep. Despite the differences, our conclusion about those tracers are consistent with each other. That is to say, in

tracer	α	β	$\log_{10}(M_{\text{turn}})$ ($h^{-1} M_{\odot}$)	$\log_{10}(\langle M_{\text{vir}} \rangle)$ ($h^{-1} M_{\odot}$)	$\langle V_{\text{peak}} \rangle$ (km s^{-1})
LRG	$0.70^{+0.01}_{-0.01}$	$1.97^{+0.01}_{-0.01}$	$13.55^{+0.00}_{-0.00}$	13.18 ± 0.01	457 ± 6
ELG	$0.76^{+0.06}_{-0.07}$	$2.16^{+0.13}_{-0.14}$	$12.05^{+0.20}_{-0.20}$	11.90 ± 0.06	159 ± 4
QSO	$0.73^{+0.07}_{-0.07}$	$2.13^{+0.05}_{-0.05}$	$12.95^{+0.10}_{-0.10}$	12.59 ± 0.03	346 ± 8

Table 4. The best-fitting α , β , M_{turn} of $\langle N_{\text{sat}} \rangle$, the mean halo mass $\langle M_{\text{vir}} \rangle$ and the mean V_{peak} (V_{peak}) for LRGs at $0.4 < z < 1.1$, ELGs at $0.8 < z < 1.6$ and QSOs at $0.8 < z < 3.5$.

DESI One-Percent Survey, LRGs are incomplete and ELGs cannot reside in the centre of the most massive haloes. We will need a more sophisticated galaxy-halo relation as well as better observations and simulations to understand this incompleteness better.

The average HOD of our SHAM satellites for all tracers can be fitted by two exponential functions of M_{vir} , i.e.,

$$\langle N_{\text{sat}} \rangle \propto \begin{cases} M_{\text{vir}}^{\alpha}, & M_{\text{vir}} > M_{\text{turn}}. \\ M_{\text{vir}}^{\beta}, & M_{\text{vir}} < M_{\text{turn}}. \end{cases} \quad (25)$$

The best-fitting results obtained by PyMULTINEST are presented in Table 4. The second exponent β at a lower mass range for all tracers is consistent and around 2. Though M_{turn} values are different for different tracers, their slope in the massive end α is well consistent with 0.7. This is consistent with ELG HOD slopes in Rocher et al. in prep but smaller than those from LRG HOD (Yuan et al. in prep).

The mean parent halo mass $\langle M_{\text{vir}} \rangle$, derived from the Monte-Carlo chain as introduced in Section 3.3, is shown in Table 4. Those values are consistent with those of ABACUS-SUMMIT HOD using the same data from the DESI One Percent Survey (Yuan et al. in prep; Rocher et al. in prep). Fig. 11 is the evolution of the mean parent halo mass for SHAM LRGs with Gaussian $v_{\text{smear,G}}$, ELGs, and QSOs. $\langle M_{\text{vir}}^{\text{LRG}} \rangle$ is not smaller than $10^{13} h^{-1} M_{\odot}$, and $\langle M_{\text{vir}}^{\text{QSO}} \rangle$ values range from $10^{12.2} h^{-1} M_{\odot}$ to $10^{12.7} h^{-1} M_{\odot}$. Both decrease with redshift, consistent with the redshift-evolution HOD results from Yuan et al. in prep. For ELG parent halo, there is no significant evolution and both $\langle M_{\text{vir}} \rangle$ are below $10^{12} h^{-1} M_{\odot}$. Rocher et al. in prep and Gao et al. in prep also find the same feature for the mean halo mass of ELGs but with slightly different values. Those are all consistent with the expectation of DESI Collaboration et al. (2016a). But the bias of ELGs still increases with redshift as indicated in Fig. 5. It should be noted that only 1.6 per cent of ELGs and less than 0.03 per cent of LRGs and QSOs reside in haloes lower than the reliable mass threshold $6 \times 10^{10} h^{-1} M_{\odot}$ (Section 2.3). So the influence of the limitation in the N -body simulation halo finder on our SHAM study can be dismissed.

The PDF of (sub)halo V_{peak} that can host a central (satellite) galaxy is shown in Fig. 12 for all three tracers at $0.8 < z < 1.1$. This is the empirical galaxy-halo relation that we calibrate using SHAM described in Section 3.2, i.e., LRG with Gaussian $v_{\text{smear,G}}$, ELG and QSO. The shape of the PDF is modulated indirectly by σ and V_{ceil} . ELGs mainly reside in (sub)haloes with $V_{\text{peak}} \lesssim 200 \text{ km s}^{-1}$, while LRG and QSOs are populated in haloes with $V_{\text{peak}} > 200 \text{ km s}^{-1}$. The PDFs of LRGs and ELGs present a clear peak, while the probability of QSOs in the massive end decays slower than them. The probability patterns for different tracers can be used as a reference for future multi-tracer studies. The mean V_{peak} values for the total LRG, ELG and QSO samples are presented in Table 4.

5 CONCLUSIONS

We have generated catalogues of mock galaxies matching the clustering of dark tracers from the DESI One Percent Survey in the range of $5\text{--}30 h^{-1} \text{ Mpc}$. The DESI samples studied here are luminous red galaxies (LRG) at $0.4 < z < 1.1$; emission line galaxies (ELG) at $0.8 < z < 1.6$ and QSO at $0.8 < z < 3.5$ (Section 2.1). Mock galaxies are painted on the dark matter only UNIT simulation (Section 2.3), using two SubHalo Abundance Matching (SHAM) algorithms (Section 3.2). The first algorithm, v_{smear} -SHAM, is used for LRGs and QSOs, and has the following free parameters: σ , to model the dispersion in the galaxy-halo mass relation but also include the incompleteness of halo mass; V_{ceil} , to account for the incompleteness of massive haloes for the galaxy samples; and v_{smear} , to model the uncertainty in the redshift determination process. The other SHAM model, f_{sat} -SHAM with a free satellite fraction f_{sat} , is introduced here to model ELGs as f_{sat} is crucial to recover the quadrupole of DESI ELGs. The redshift uncertainty of ELGs is the lowest among the considered tracers and its v_{smear} has a negligible impact on the clustering of SHAM ELGs down to $5 h^{-1} \text{ Mpc}$. So v_{smear} is not included in f_{sat} -SHAM.

For LRGs, we find the best-fitting σ to be consistent with 0 at a $2\text{-}\sigma$ level. However, ELG and QSO samples constrain σ weakly. Although the loose constraint from the QSO sample is mostly due to its small number density, this does not stand for ELGs which are over 10 times denser than QSOs. We attribute this lack of constraint to the fact that σ also models the incompleteness in both stellar mass and luminosity, resulting in a complex galaxy-halo relation that is harder to constrain.

V_{ceil} , the massive-(sub)halo incompleteness, describes the stellar mass incompleteness in the massive end due to both target selection criteria of galaxy surveys and the intrinsic properties of certain galaxies. The best-fitting V_{ceil} for LRGs, is as small as 0.02 per cent. This small value shows that DESI LRGs from the One Percent Survey are close to complete at the massive end. The best fit V_{ceil} for ELGs shows that up to 7 per cent of (sub)haloes that have the largest V_{scat} (Eq. (13)) in the UNIT simulation would not host ELGs. Although QSOs are the brightest object at $z > 1$, their best-fitting V_{ceil} is inconsistent with zero, suggesting that not all haloes above a certain mass will be hosting a QSO. Their absence in the centre of massive (sub)haloes is consistent with the depletion of cold gas in this hot and dense environment there, leading to the quenching of ELG star formation and QSO black hole accretion. This agrees with the scenarios found in SAM studies and observations (e.g., Uchiyama et al. 2018; Griffin et al. 2019; Gonzalez-Perez et al. 2020).

v_{smear} quantifies the effect that the redshift uncertainty has on the clustering. It can also be measured statistically and independently by the redshift difference Δv of repeat observations (see Section 2.2). The Δv histogram of DESI tracers follows, in general, a Lorentzian profile with width $w_{\Delta v}$, instead of a single Gaussian profile as was found for BOSS/eBOSS galaxies. Thus, we have developed SHAM algorithms with a truncated Lorentzian profile for modelling the redshift uncertainty, i.e., $v_{\text{smear,L}}$. The Δv of LRG sub-samples in different redshift bins can be fitted well by a Lorentzian or a Gaussian profile and thus, we also develop a Gaussian $v_{\text{smear,G}}$ for LRGs. The Lorentzian $v_{\text{smear,L}}$ of LRGs is only consistent with $w_{\Delta v}$ at $0.4 < z < 1.1$. The clustering of LRG sub-samples in redshift bins actually suggests a preference for a Gaussian profile for the redshift uncertainty. Nevertheless, truncated Lorentzian and Gaussian functions provide the same SHAM clustering and consistent best-fitting σ and V_{ceil} . For QSOs, $v_{\text{smear,L}}$ monotonically increases and deviates from $w_{\Delta v}$ at $z > 1.5$. This is because the C IV line used to determine

QSO redshifts is affected by the velocity shifts of spectral lines that can vary between objects. Although the repeat observation cannot capture this feature, its effect on the clustering will be modelled by SHAM $v_{\text{smear,L}}$. This is consistent with the eBOSS QSO analysis (Zarrouk et al. 2018).

The satellite fraction f_{sat} of LRG and QSO samples is fixed to the number of subhaloes from the UNIT simulation included for the SHAM, given σ and V_{ceil} . Their f_{sat} decreases with redshift, following the evolution of the subhalo fraction in the simulations. For ELGs we use the f_{sat} -SHAM, setting f_{sat} as a free parameter. The best-fitting f_{sat} for DESI ELGs is around 4 per cent. This low value is consistent with previous studies for strong [O II] emitters (Gonzalez-Perez et al. 2020; Gao et al. 2022), but it is lower than the estimations for the total ELG samples (Favole et al. 2016; Guo et al. 2019; Lin et al. 2023).

We provide the average halo occupation distribution (HOD) measured from our best-fitting SHAM for LRGs, ELGs and QSOs from the One Percent Survey. The HOD of SHAM central LRGs reaches its peak at $\langle N \rangle = 0.75 \pm 0.07$ and decreases at the massive end as $V_{\text{ceil}} \neq 0$. The HOD for central SHAM ELGs is consistent with a star-forming HOD profile peaking at $\langle N_{\text{cen}} \rangle = 0.06 \pm 0.03$ and $M_{\text{vir}} = 10^{11.7} h^{-1} M_{\odot}$, but we cannot exclude a Gaussian shape (e.g. Avila et al. 2020). The HOD for SHAM central QSO also decreases after $M_{\text{vir}} = 10^{12.4} h^{-1} M_{\odot}$ with $\langle N \rangle = 0.016 \pm 0.001$. The HOD for all types of SHAM satellite galaxies is composed of two exponential functions with different slopes. The slope α in the massive halo end is $\alpha_{\text{LRG}} = 0.70^{+0.01}_{-0.01}$, $\alpha_{\text{ELG}} = 0.76^{+0.06}_{-0.07}$, and $\alpha_{\text{QSO}} = 0.73^{+0.07}_{-0.07}$. They are smaller than the measurements from ABACUS-SUMMIT HOD tests for LRGs but consistent with those from ELGs and QSOs (Yuan et al. in prep; Rocher et al. in prep).

We measure a mean parent halo mass of $\langle M_{\text{vir}} \rangle = 10^{13.16 \pm 0.01} h^{-1} M_{\odot}$ for LRGs, $10^{11.90 \pm 0.06} h^{-1} M_{\odot}$ for ELGs and $10^{12.66 \pm 0.45} h^{-1} M_{\odot}$ for QSOs. For sub-samples at redshift bins, we obtain $\langle M_{\text{vir}} \rangle$ that decreases with redshift for LRGs and QSOs, but not for ELGs. Meanwhile, the linear bias for each tracer increases with the redshift. Those results are consistent with the HOD measurement using the same tracers from the One Percent Survey in general.

We also provide the SHAM-calibrated probability distribution of V_{peak} for LRGs, ELGs and QSOs at $0.8 < z < 1.1$. LRGs and QSOs are populated in (sub)haloes with a similar range of V_{peak} , $\langle V_{\text{peak,LRG}} \rangle = 457 \pm 6 \text{ km s}^{-1}$ and $\langle V_{\text{peak,QSO}} \rangle = 346 \pm 8 \text{ km s}^{-1}$. The value for ELG (sub)haloes is smaller, $\langle V_{\text{peak,ELG}} \rangle = 159 \pm 4 \text{ km s}^{-1}$. This result will be useful for future multi-tracer studies.

SHAM algorithms that include the redshift uncertainty, massive-(sub)halo incompleteness and an adjustable satellite fraction work well in the single-tracer case, which can provide galaxy mocks for cosmological tests. We plan to enhance this study in the future by implementing a multi-tracer SHAM method based on what we have learnt from the present study.

DATA AVAILABILITY

All the figures and the best-fitting mock galaxies of SHAM are available in Zenodo: <https://doi.org/10.5281/zenodo.7993414>.

ACKNOWLEDGEMENTS

JY, CZ and JPK acknowledge support from the SNF 200020_175751 and 200020_207379 ‘‘Cosmology with 3D Maps of the Universe’’ research grant. VGP is supported by the Atracci3n de Talento Contract no. 2019-TI/TIC-12702 granted by the Comunidad de Madrid in Spain and by the Ministerio de Ciencia e Innovaci3n (MICINN) under research grant PID2021-122603NB-C21. We would like to thank Risa Wechsler, Christophe Y3che, Zheng Zheng, Charling Tao, Philip Mansfield, Hong Guo, Cheng Li, Haowen Zhang and Xiangyu Jin for their helpful discussions. We also thank John Helly for providing us with the Millennium simulation.

This material is based upon work supported by the U.S. Department of Energy (DOE), Office of Science, Office of High-Energy Physics, under Contract No. DE-AC02-05CH11231, and by the National Energy Research Scientific Computing Center, a DOE Office of Science User Facility under the same contract. Additional support for DESI was provided by the U.S. National Science Foundation (NSF), Division of Astronomical Sciences under Contract No. AST-0950945 to the NSF’s National Optical-Infrared Astronomy Research Laboratory; the Science and Technologies Facilities Council of the United Kingdom; the Gordon and Betty Moore Foundation; the Heising-Simons Foundation; the French Alternative Energies and Atomic Energy Commission (CEA); the National Council of Science and Technology of Mexico (CONACYT); the Ministry of Science and Innovation of Spain (MICINN), and by the DESI Member Institutions: <https://www.desi.lbl.gov/collaborating-institutions>. Any opinions, findings, and conclusions or recommendations expressed in this material are those of the author(s) and do not necessarily reflect the views of the U. S. National Science Foundation, the U. S. Department of Energy, or any of the listed funding agencies.

The authors are honoured to be permitted to conduct scientific research on Iolkam Du’ag (Kitt Peak), a mountain with particular significance to the Tohono O’odham Nation.

REFERENCES

- Alam S., Peacock J. A., Kraljic K., Ross A. J., Comparat J., 2020, *MNRAS*, **497**, 581
- Alam S., et al., 2021a, *Phys. Rev. D*, **103**, 083533
- Alam S., et al., 2021b, *MNRAS*, **504**, 4667
- Alexander D. M., et al., 2023, *AJ*, **165**, 124
- Allende Prieto C., et al., 2020, *Research Notes of the American Astronomical Society*, **4**, 188
- Angulo R. E., Pontzen A., 2016, *MNRAS*, **462**, L1
- Avila S., et al., 2020, *MNRAS*, **499**, 5486
- Bailey et al. in prep.
- Bautista J. E., et al., 2021, *MNRAS*, **500**, 736
- Behroozi P. S., Conroy C., Wechsler R. H., 2010, *ApJ*, **717**, 379
- Behroozi P. S., Wechsler R. H., Wu H.-Y., 2013a, *ApJ*, **762**, 109
- Behroozi P. S., Wechsler R. H., Wu H.-Y., Busha M. T., Klypin A. A., Primack J. R., 2013b, *ApJ*, **763**, 18
- Behroozi P., Wechsler R. H., Hearin A. P., Conroy C., 2019, *MNRAS*, **488**, 3143
- Bianchi D., Percival W. J., 2017, *MNRAS*, **472**, 1106
- Blanton M. R., et al., 2017, *AJ*, **154**, 28
- Buchner J., et al., 2014, *A&A*, **564**, A125
- Chaussidon E., et al., 2022, arXiv e-prints, p. arXiv:2208.08511
- Chuang C.-H., et al., 2019, *MNRAS*, **487**, 48
- Conroy C., Wechsler R. H., Kravtsov A. V., 2006, *ApJ*, **647**, 201
- Contreras S., Angulo R. E., Zennaro M., 2021, *MNRAS*, **508**, 175
- Cooper A. P., et al., 2022, arXiv e-prints, p. arXiv:2208.08514
- DESI Collaboration et al., 2016a, The DESI Experiment Part I: Science, Targeting, and Survey Design (arXiv:1611.00036)

- DESI Collaboration et al., 2016b, The DESI Experiment Part II: Instrument Design ([arXiv:1611.00037](https://arxiv.org/abs/1611.00037))
- DESI Collaboration et al., 2022, *AJ*, 164, 207
- DESI Collaboration et al. 2023a, *Phys. Rev. D*
- DESI Collaboration et al. 2023b
- Dawson K. S., et al., 2012, *AJ*, 145, 10
- Dawson K. S., et al., 2016, *AJ*, 151, 44
- DeRose J., Becker M. R., Wechsler R. H., 2022, *ApJ*, 940, 13
- Dekel A., Birnboim Y., 2006, *MNRAS*, 368, 2
- Dey A., et al., 2019, *AJ*, 157, 168
- Eisenstein D. J., Hu W., 1998, *ApJ*, 496, 605
- Eisenstein D. J., et al., 2011, *AJ*, 142, 72
- Favole G., et al., 2016, *MNRAS*, 461, 3421
- Favole G., Montero-Dorta A. D., Artale M. C., Contreras S., Zehavi I., Xu X., 2022, *MNRAS*, 509, 1614
- Feldman H. A., Kaiser N., Peacock J. A., 1994, *ApJ*, 426, 23
- Feroz F., Hobson M. P., 2008, *MNRAS*, 384, 449
- Feroz F., Hobson M. P., Bridges M., 2009, *MNRAS*, 398, 1601
- Feroz F., Hobson M. P., Cameron E., Pettitt A. N., 2019, *OJAp*, 2, 10
- Gao H., Jing Y. P., Zheng Y., Xu K., 2022, *ApJ*, 928, 10
- Gaskell C. M., 1982, *ApJ*, 263, 79
- Gonzalez-Perez V., Lacey C. G., Baugh C. M., Lagos C. D. P., Helly J., Campbell D. J. R., Mitchell P. D., 2014, *MNRAS*, 439, 264
- Gonzalez-Perez V., et al., 2018, *MNRAS*, 474, 4024
- Gonzalez-Perez V., et al., 2020, *MNRAS*, 498, 1852
- Griffin A. J., Lacey C. G., Gonzalez-Perez V., Lagos C. d. P., Baugh C. M., Fanidakis N., 2019, *MNRAS*, 487, 198
- Guo H., et al., 2015, *MNRAS*, 453, 4368
- Guo H., et al., 2019, *ApJ*, 871, 147
- Guy J., et al., 2023, *AJ*, 165, 144
- Hadzhiyska B., Tacchella S., Bose S., Eisenstein D. J., 2021, *MNRAS*, 502, 3599
- Hahn C., et al., 2022, [arXiv e-prints](https://arxiv.org/abs/2208.08512), p. [arXiv:2208.08512](https://arxiv.org/abs/2208.08512)
- Hartlap J., Simon P., Schneider P., 2007, *A&A*, 464, 399
- Hearin A. P., Zentner A. R., Berlind A. A., Newman J. A., 2013, *Monthly Notices of the Royal Astronomical Society*, 433, 659
- Hou J., et al., 2018, *MNRAS*, 480, 2521
- Ishiyama T., et al., 2021, *MNRAS*, 506, 4210
- Jing Y., 2019, *Science China Physics, Mechanics, and Astronomy*, 62, 19511
- Kaiser N., 1987, *MNRAS*, 227, 1
- Kauffmann G., White S. D. M., Heckman T. M., Ménard B., Brinchmann J., Charlot S., Tremonti C., Brinkmann J., 2004, *MNRAS*, 353, 713
- Kitaura F.-S., et al., 2016, *MNRAS*, 456, 4156
- Kravtsov A. V., Berlind A. A., Wechsler R. H., Klypin A. A., Gottlober S., Allgood B., Primack J. R., 2004, *ApJ*, 609, 35
- Lan T.-W., et al., 2023, *ApJ*, 943, 68
- Landy S. D., Szalay A. S., 1993, *ApJ*, 412, 64
- Lasker J., et al., in prep.
- Leauthaud A., et al., 2012, *ApJ*, 744, 159
- Lehmann B. V., Mao Y.-Y., Becker M. R., Skillman S. W., Wechsler R. H., 2017, *ApJ*, 834, 37
- Levi M., et al., 2013, [arXiv e-prints](https://arxiv.org/abs/1308.0847), p. [arXiv:1308.0847](https://arxiv.org/abs/1308.0847)
- Lewis A., 2019, [arXiv e-prints](https://arxiv.org/abs/1910.13970), p. [arXiv:1910.13970](https://arxiv.org/abs/1910.13970)
- Lin S., Tinker J. L., Blanton M. R., Guo H., Raichoor A., Comparat J., Brownstein J. R., 2023, *MNRAS*, 519, 4253
- Lyke B. W., et al., 2020, *ApJS*, 250, 8
- Maksimova N. A., Garrison L. H., Eisenstein D. J., Hadzhiyska B., Bose S., Satterthwaite T. P., 2021, *MNRAS*, 508, 4017
- Miller et al. in prep.
- Mohammad F. G., et al., 2020, *MNRAS*, 498, 128–143
- Moustakas et al. in prep.
- Myers A. D., et al., 2023, *AJ*, 165, 50
- Parejko J. K., et al., 2013, *MNRAS*, 429, 98
- Peebles P. J. E., Hauser M. G., 1974, *ApJS*, 28, 19
- Peng Y.-j., et al., 2010, *ApJ*, 721, 193
- Percival W. J., Bianchi D., 2017, *MNRAS*, 472, L40
- Planck Collaboration et al., 2016, *A&A*, 594, A13
- Prada F., Klypin A. A., Cuesta A. J., Betancort-Rijo J. E., Primack J., 2012, *MNRAS*, 423, 3018
- Raichoor A., et al., 2020, *Research Notes of the American Astronomical Society*, 4, 180
- Raichoor A., et al., 2023, *AJ*, 165, 126
- Raichoor et al. in prep.
- Reddick R. M., Wechsler R. H., Tinker J. L., Behroozi P. S., 2013, *ApJ*, 771, 30
- Richards G. T., Vanden Berk D. E., Reichard T. A., Hall P. B., Schneider D. P., SubbaRao M., Thakar A. R., York D. G., 2002, *AJ*, 124, 1
- Richards G. T., et al., 2011, *AJ*, 141, 167
- Rodríguez-Torres S. A., et al., 2016, *MNRAS*, 460, 1173
- Rodríguez-Torres S. A., et al., 2017, *MNRAS*, 468, 728
- Rosario D. J., et al., 2013, *A&A*, 560, A72
- Ross A. J., et al., 2014, *MNRAS*, 437, 1109
- Ross A. J., et al., 2020, *MNRAS*, 498, 2354
- Ruiz-Macias O., et al., 2020, *Research Notes of the American Astronomical Society*, 4, 187
- Schlafly E., et al., in prep.
- Schlegel et al. in prep.
- Shen Y., et al., 2016, *ApJ*, 831, 7
- Silber J. H., et al., 2022, *AJ*, 165, 9
- Sinha M., Garrison L., 2019, in Majumdar A., Arora R., eds, *Software Challenges to Exascale Computing*. Springer Singapore, Singapore, pp 3–20
- Sinha M., Garrison L. H., 2020, *MNRAS*, 491, 3022
- Smith A., et al., 2020, *MNRAS*, 499, 269
- Smith A., de Mattia A., Burtin E., Chuang C.-H., Zhao C., 2021, *MNRAS*, 500, 259
- Springel V., et al., 2005, *Nature*, 435, 629
- Steinmetz M., Navarro J., 1999, *ApJ*, 513, 555
- Tasitsiomi A., Kravtsov A. V., Wechsler R. H., Primack J. R., 2004, *ApJ*, 614, 533
- Tinker J., Wetzel A., Conroy C., 2011, [arXiv e-prints](https://arxiv.org/abs/1107.5046), p. [arXiv:1107.5046](https://arxiv.org/abs/1107.5046)
- Trujillo-Gomez S., Klypin A., Primack J., Romanowsky A. J., 2011, *ApJ*, 742, 16
- Uchiyama H., et al., 2018, *PASJ*, 70, S32
- Wang Y., Chuang C.-H., Hirata C. M., 2013, *MNRAS*, 430, 2446
- Weinberger R., et al., 2018, *MNRAS*, 479, 4056
- Wetzel A. R., Tinker J. L., Conroy C., 2012, *MNRAS*, 424, 232
- Willick J. A., Courteau S., Faber S. M., Burstein D., Dekel A., Strauss M. A., 1997, *ApJS*, 109, 333
- Yèche C., et al., 2020, *Research Notes of the American Astronomical Society*, 4, 179
- Yu J., et al., 2022, *MNRAS*, 516, 57
- Zarrouk P., et al., 2018, *MNRAS*, 477, 1639
- Zhai Z., et al., 2017, *ApJ*, 848, 76
- Zhao C., et al., 2021, *MNRAS*, 503, 1149
- Zheng Z., et al., 2005, *ApJ*, 633, 791
- Zhou R., et al., 2020, *Research Notes of the American Astronomical Society*, 4, 181
- Zhou R., et al., 2023, *AJ*, 165, 58
- Zou H., et al., 2017, *PASP*, 129, 064101
- van den Bosch F. C., Ogiya G., 2018, *MNRAS*, 475, 4066
- van den Bosch F. C., Ogiya G., Hahn O., Burkert A., 2018, *MNRAS*, 474, 3043

APPENDIX A: 4-PARAMETER SHAM

SHAM with 4 parameters $\{\sigma, V_{\text{ceil}}, v_{\text{smear}}, f_{\text{sat}}\}$ is the inclusive version of v_{smear} -SHAM and f_{sat} -SHAM. Fig. A1 provides the impact of those 4 parameters on the 2PCF monopole, quadrupole and projected 2PCF of UNIT-SHAM galaxies in the fitting range $5\text{--}30 h^{-1}$ Mpc. The ‘standard’ clustering is obtained from $\sigma, V_{\text{ceil}}, v_{\text{smear}} = 0$ using v_{smear} -SHAM. So its f_{sat} is derived from its SHAM catalogue. When we have a larger σ as shown in the first column of Fig. A1, ξ_0 and w_p decrease and ξ_2 rotates counter-clock-wise with respect to a point at

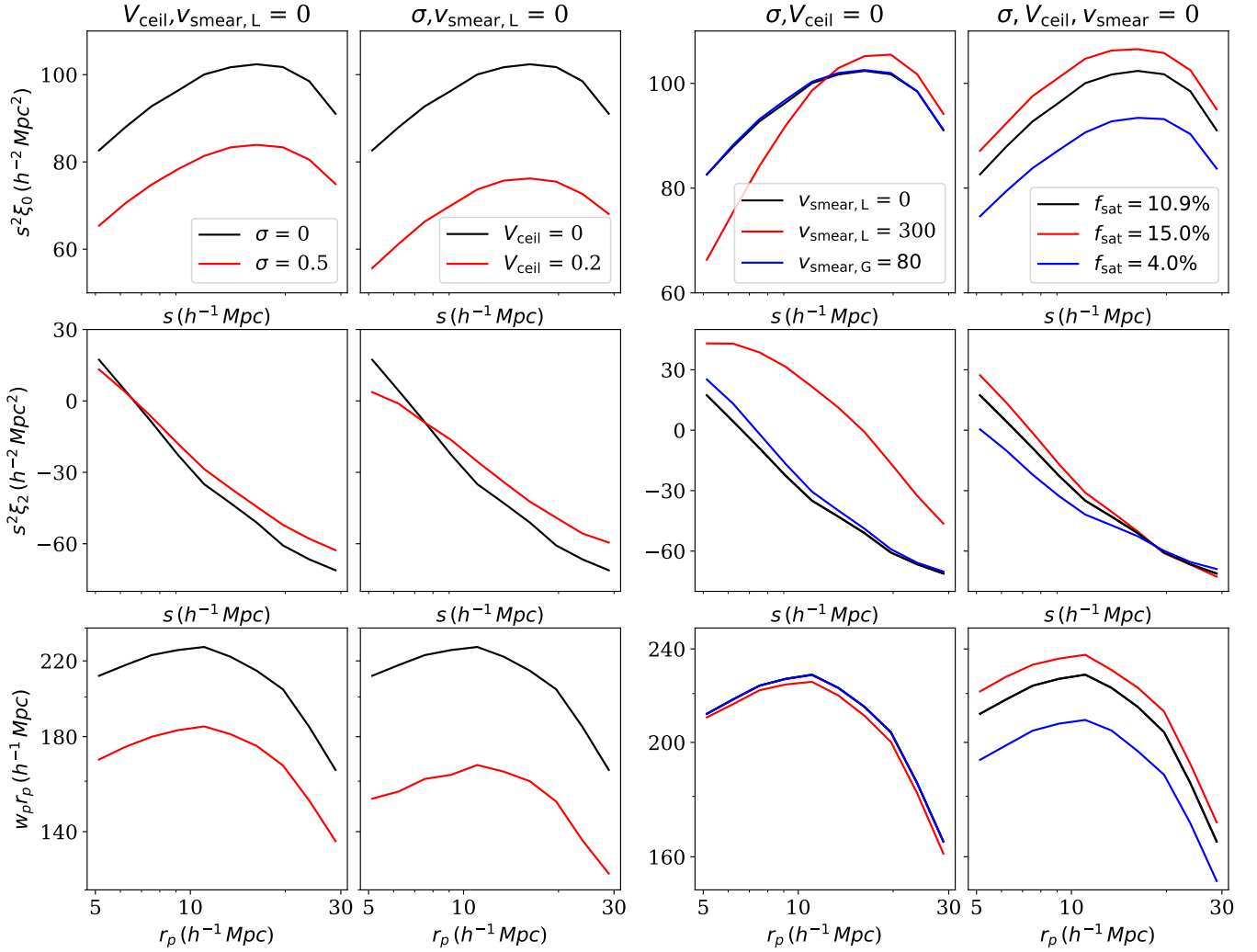


Figure A1. The impact of σ (first column), V_{ceil} (second column), v_{smear} (third column), f_{sat} (fourth column) on the 2PCF monopole (first row), quadrupole (second row) and the projected 2PCF (third row). The standard sample is $\sigma, V_{\text{ceil}}, v_{\text{smear}} = 0$ with $f_{\text{sat}} = 10.9$ per cent in black lines. The first three columns show the 2PCF difference between the standard sample and samples with $\sigma = 0.5$, $V_{\text{ceil}} = 0.2$ per cent or $v_{\text{smear,L}} = 300 \text{ km s}^{-1}$ (truncated at 2000 km s^{-1}) respectively while fixing the other two parameters, in red lines. Results of v_{smear} -SHAM with a Gaussian profile $v_{\text{smear,G}} = 80 \text{ km s}^{-1}$ are also presented in the third column in blue lines. In the last column, we compare the 2PCF for SHAM galaxies with $f_{\text{sat}} = 15$ per cent (red lines) and $f_{\text{sat}} = 4$ per cent (blue lines) with that of the standard sample in f_{sat} -SHAM with $\sigma, V_{\text{ceil}}, v_{\text{smear}} = 0$.

redshift range	z_{eff}	z_{UNIT}	V_{eff} ($h^{-3} \text{ Gpc}^3$)	$10^4 n_{\text{eff}}$ ($h^3 \text{ Mpc}^{-3}$)	σ	$v_{\text{smear,G}}$ (km s^{-1})	V_{ceil} (%)	f_{sat} (%)	χ^2/dof
$0.2 < z < 0.43$	0.3441	0.3337	0.62	2.95	$0.19^{+0.06}_{-0.06}$	63^{+45}_{-37}	$0.0045^{+0.0048}_{-0.0030}$	$13.55^{+2.07}_{-3.13}$	51/37
$0.2 < z < 0.33$	0.2754	0.2760	0.29	3.37	$0.15^{+0.09}_{-0.10}$	58^{+40}_{-38}	$0.0077^{+0.0060}_{-0.0048}$	$15.87^{+1.81}_{-3.11}$	32/37
$0.33 < z < 0.43$	0.3865	0.3941	0.33	2.58	$0.27^{+0.05}_{-0.07}$	36^{+48}_{-28}	$0.0030^{+0.0038}_{-0.0021}$	$13.48^{+1.13}_{-2.66}$	50/37

Table A1. The same as Table 2 but for 4-parameter SHAM with $\{\sigma, V_{\text{ceil}}, v_{\text{smear}}, f_{\text{sat}}\}$ applied on BOSS LOWZ clustering at $0.2 < z < 0.43$.

$s \sim 6 h^{-1} \text{ Mpc}$. A larger V_{ceil} leads to a similar effect as shown in the second column, with the rotating point moving to $s \sim 7 h^{-1} \text{ Mpc}$. v_{smear} and f_{sat} are another pair of parameters that can change the velocity distribution along the line of sight, thus degenerated with each other. As presented in the third column of Fig. A1, increasing v_{smear} causes a larger ξ_2 on $5\text{--}30 h^{-1} \text{ Mpc}$. A Gaussian $v_{\text{smear,G}}$ does not have a huge impact on ξ_0 and w_p , while a Lorentzian profile

$v_{\text{smear,L}}$ with a truncation in 2000 km s^{-1} does influence ξ_0 . Note that the clustering effect of a Lorentzian profile can be similar to that of a Gaussian profile as shown in Section 4.4. The difference in the clustering effect here should be attributed to both the v_{smear} value and truncation value. Nonetheless, those two symmetric v_{smear} profiles can only lead to an increasing ξ_2 at $5\text{--}30 h^{-1} \text{ Mpc}$ for SHAM galaxies compared to that of the ‘standard’ sample. In contrast, we can

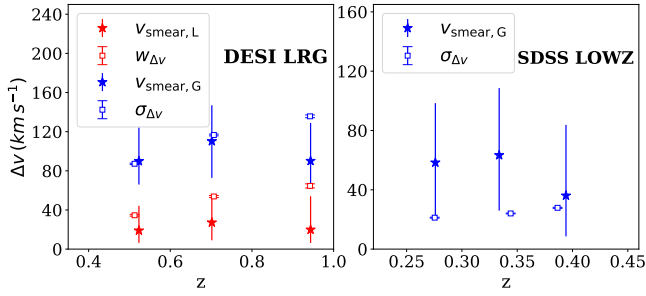


Figure A2. The redshift uncertainty measured from repeat observation (filled stars with error bars) and from SHAM (empty squares with error bars) for 4-parameter SHAM for LRGs (left panel) and SDSS-III LOWZ (right panel). Results for Lorentzian profiles are presented in red and those of Gaussian profiles are in blue. Note that the Gaussian measurements for DESI LRGs are shifted by 40 km s^{-1} upwards.

decrease ξ_2 w.r.t. the ‘standard’ one at similar scales by decreasing f_{sat} . Note that those are the critical scales to reproduce the clustering of DESI ELG. Varying f_{sat} results in a systematical shift for ξ_0 and w_p as well.

We apply the 4-parameter SHAM to LRGs from the One Percent Survey for a consistency check with v_{smear} SHAM. We also perform a SHAM test for SDSS-III BOSS LOWZ samples, trying to resolve the overestimation of redshift uncertainty by v_{smear} -SHAM found in Yu22. In Fig. A2, we present the v_{smear} from the best-fitting 4-parameter SHAM together with $w_{\Delta v}$ and $\sigma_{\Delta v}$ from the repeat observations for DESI LRGs (left) and LOWZ LRG samples (right). Comparing with Fig. 6, v_{smear} values systematically shift to smaller values. The satellite fraction of 4-parameter SHAM is consistent with that of v_{smear} -SHAM, except for LRGs at $0.8 < z < 1.1$ with Gaussian profile, for which the $v_{\text{smear,G}}$ result becomes inconsistent with $\sigma_{\Delta v}$ of repeat observations. As we have a reliable statistical measurement of LRG redshift uncertainty, it means that the satellite fraction estimation might be biased by the redshift uncertainty.

For the LOWZ 4-parameter SHAM study, the basic information of LOWZ observation, including UNIT simulations and the best-fitting SHAM results is presented in Table A1. Our best-fitting v_{smear} are consistent with $\sigma_{\Delta v}$, resolving the discrepancy shown in Figure 6 of Yu22. The $v_{\text{smear}}-f_{\text{sat}}$ degeneracy enables v_{smear} to decrease to the observed uncertainty level by increasing its satellite fraction. Meanwhile, our best-fitting f_{sat} is consistent with the LOWZ HOD $f_{\text{sat}} = 12 \pm 2$ per cent (Parejko et al. 2013).

APPENDIX B: POSTERIOR CONTOURS

In Figures B1–B4, we present the posteriors of the fittings from Table 2, i.e., those of v_{smear} -SHAM for LRG samples and QSOs, and f_{sat} -SHAM for ELG samples. The v_{smear} profile here is Lorentzian. They are plotted using GETDIST (Lewis 2019). All fittings have converged and are ended by the nested sampling automatically.

APPENDIX C: REPRODUCED w_p

We provide the comparison between mock galaxies of SHAM and observations for the projected 2PCF $w_p r_p$ at $5-30 h^{-1}$ Mpc in Figures C1–C3. The mock galaxies are constructed using the parameter set of SHAM that corresponds to the minimum χ^2 . The π_{max} of their w_p are $30 h^{-1}$ Mpc (Section 3.1). The best-fitting reduced χ^2

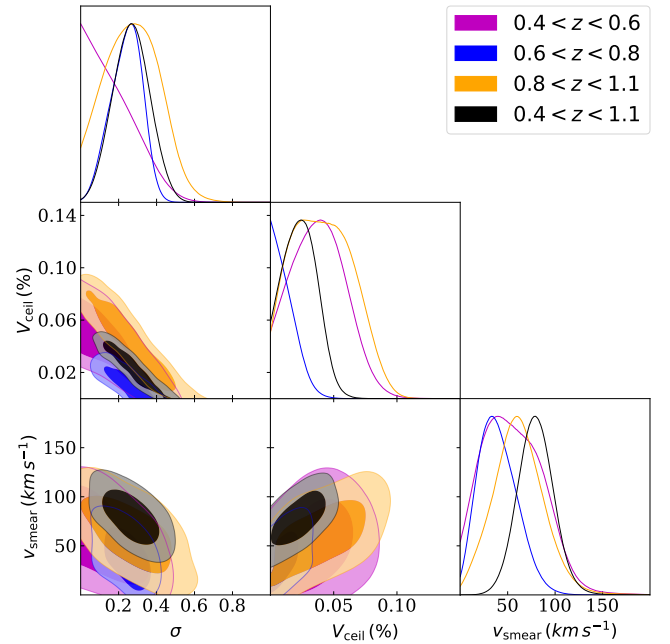


Figure B1. The posterior corner plot for LRGs at $0.4 < z < 0.6$ (magenta), $0.6 < z < 0.8$ (blue), $0.8 < z < 1.1$ (orange), and $0.4 < z < 1.1$ (grey). The parameters are σ , V_{cell} , v_{smear} .

of LRG at $0.8 < z < 1.1$ is larger than 1.5, but the reproduced w_p agrees with the observation. So mock galaxies of SHAM for this sample are still a good description of the observed clustering.

We note the disagreement on scales smaller than $1 h^{-1}$ Mpc between the observation and the prediction of the best-fitting SHAM galaxy mocks in general as illustrated in Fig. C4. This is probably due to the over-disruption or over-merging of subhaloes in N -body simulations (e.g., van den Bosch & Ogiya 2018; van den Bosch et al. 2018; Behroozi et al. 2019). In addition to that, the uprising small-scale $w_p r_p$ of DESI ELGs may have physical explanations as shown in Roher et al. in prep.

APPENDIX D: IS SATELLITE FRACTION BIASED?

To test whether our satellite fraction in f_{sat} -SHAM is unbiased or not, we compare its best-fitting value with the true value provided by mock galaxies constructed in various galaxy–halo models. The definition of satellite fraction for those ELG samples should be the same as f_{sat} in f_{sat} -SHAM. We apply SHAM on N -body simulations that are used for producing those galaxy catalogues and fit the 2PCF monopole and quadrupole of those modelled galaxies on $5-30 h^{-1}$ Mpc. Their covariance matrices are obtained from jackknife subsamples produced by PYCORR.

The first set of galaxies is from a DESI-like ELG catalogue from SAM (Gonzalez-Perez et al. 2014, 2020, SAM ELG hereafter) at redshift $z = 0.99$ with $f_{\text{sat}} = 4.56$ per cent. The corresponding N -body simulation is MILLENNIUM⁹ with the WMAP7 cosmology (Springel et al. 2005). As there is no V_{peak} in this simulation, we use V_{max} for f_{sat} -SHAM. Another sample of star-forming galaxies

⁹ https://virgodb.dur.ac.uk:8443/Millennium/Help?page=data_bases/gonzalez2014a/mr7

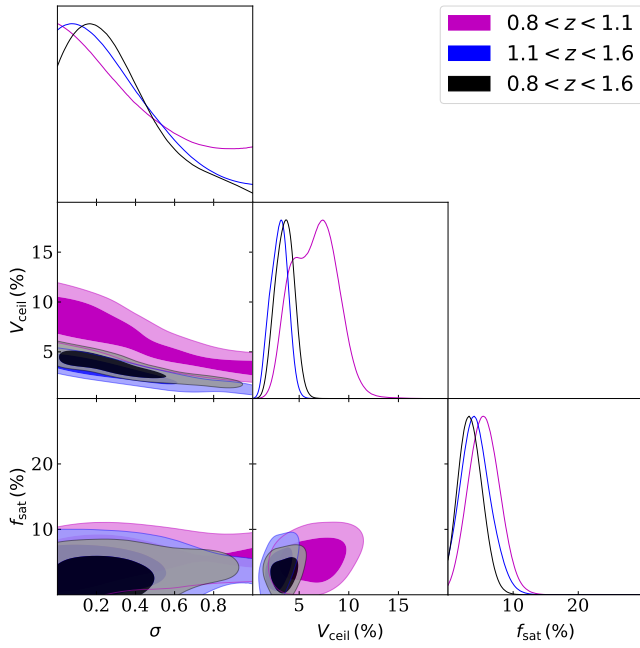


Figure B2. The posterior corner plot for ELGs at $0.8 < z < 1.1$ (magenta), $1.1 < z < 1.6$ (blue) and $0.8 < z < 1.6$ (grey). The parameters are σ , V_{cell} , f_{sat} .

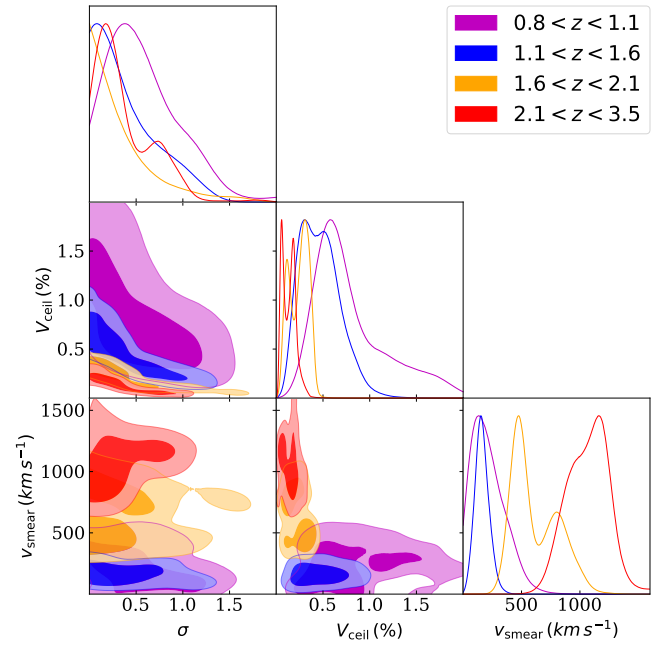


Figure B4. The same as Fig. B1 but for QSOs at $0.8 < z < 1.1$ (magenta), $1.1 < z < 1.6$ (blue), $1.6 < z < 2.1$ (orange), and $2.1 < z < 3.5$ (red).

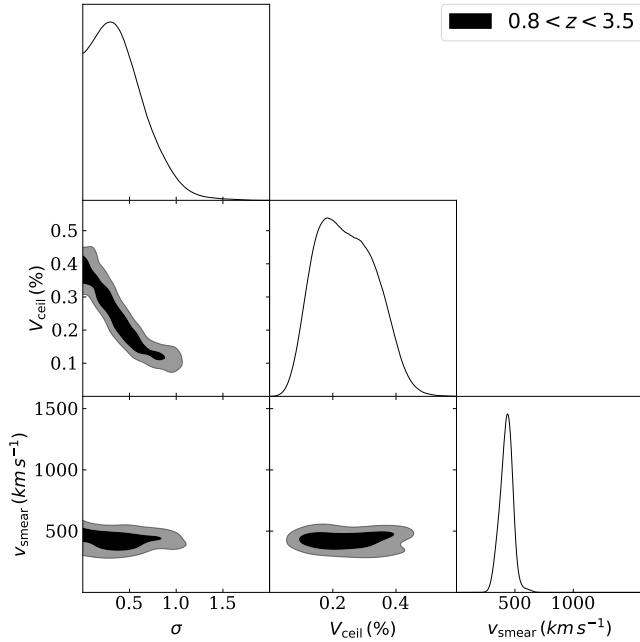


Figure B3. The same as Fig. B1 but for QSOs at $0.8 < z < 3.5$.

from UniverseMachine (Behroozi et al. 2019, UniverseMachine ELG hereafter) at $z = 0.9436$ with satellite fraction $f_{\text{sat}} = 17.75$ per cent. UniverseMachine ELGs have a star-formation rate larger than $10^{1.1} M_{\odot} \text{yr}^{-1}$ and $10^{9.6} < M_{*} < 10^{11} M_{\odot}$. We finally downsample UniverseMachine ELGs to have $n_{\text{gal}} = 9.64 \times 10^{-4} \text{Mpc}^{-3} h^3$, similar to that of DESI ELGs at $0.8 < z < 1.1$. This galaxy catalogue is

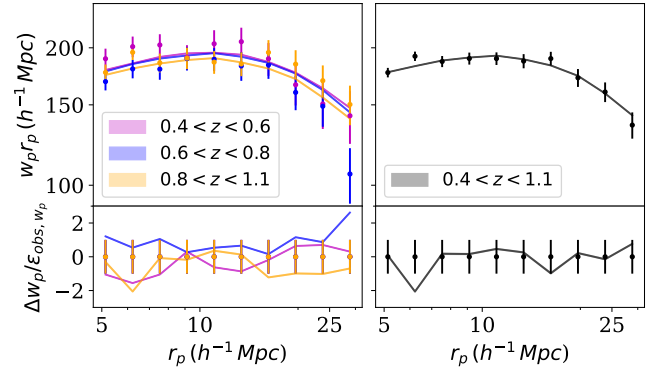


Figure C1. The projected 2PCFs $w_p r_p$ of observed LRGs (filled circles with error bars) and those of the best-fitting SHAM galaxies (solid lines with shades) with $\pi_{\text{max}} = 30 h^{-1} \text{Mpc}$. The direct comparison and residuals rescaled by the observed error bars are presented in the first and the second row respectively. The samples on the left are LRGs at different redshift bins, while the sample on the right is the total sample.

based on the snapshot of MULTIDARK MDPL2 simulation (Prada et al. 2012) at the same redshift¹⁰.

Fig. D1 shows the clustering of SAM ELGs (blue dots with error bars), UniverseMachine ELGs (magenta dots with error bars) and DESI ELGs (black dots with error bars), and the clustering of the best-fitting SHAM galaxies (lines with corresponding colours). Our f_{sat} -SHAM can fit the 2PCF multipoles for SAM ELGs and UniverseMachine ELGs and can reproduce their projected 2PCF on $5\text{--}30 h^{-1} \text{Mpc}$. The best-fitting f_{sat} for SAM ELGs is $7.47^{+0.94}_{-0.82}$ per cent, which is a more than $3\text{-}\sigma$ overestimation. Meanwhile, that for

¹⁰ <https://www.cosmosim.org/metadata/mdpl2/>

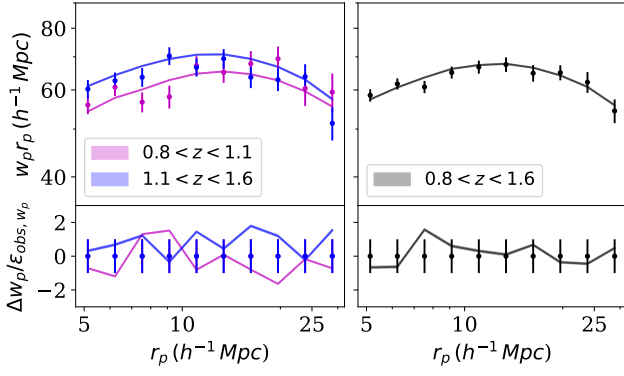


Figure C2. Same as Fig. C1 but for ELGs.

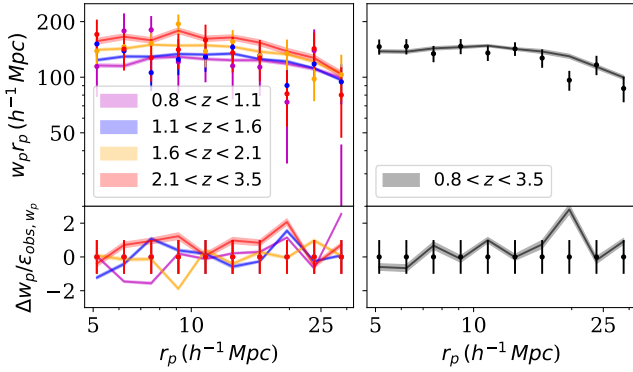


Figure C3. Same as Fig. C1 but for QSOs.

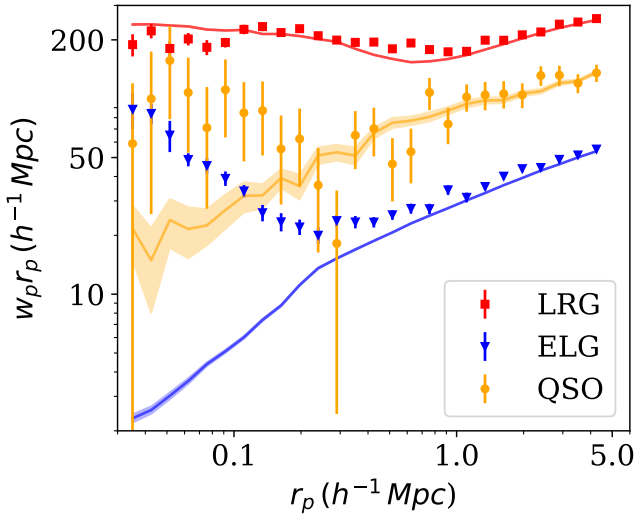


Figure C4. The projected 2PCF $w_p r_p$ at $0.01\text{--}5 h^{-1} \text{Mpc}$ of observations (filled error bars) and the predictions from the best-fitting SHAM (solid lines with shades). Among the filled error bars, red squares are for LRGs, blue triangles are for ELGs and yellow circles are for QSOs. The colour of the solid lines with shades is the same as the colour of the corresponding error bars. The $w_p r_p$ of LRGs is vertically shifted.

UniverseMachine ELGs is $13.05^{+0.86}_{-0.77}$ per cent, a more than $5\text{-}\sigma$ underestimation. The underestimation of the UniverseMachine satellite fraction is partly due to their reconstructed orphan galaxies which we do not have in our SHAM satellites. However, the inconsistency in the estimation of the satellite fraction among different galaxy–halo models needs further discussion in future studies.

This paper has been typeset from a \LaTeX file prepared by the author.

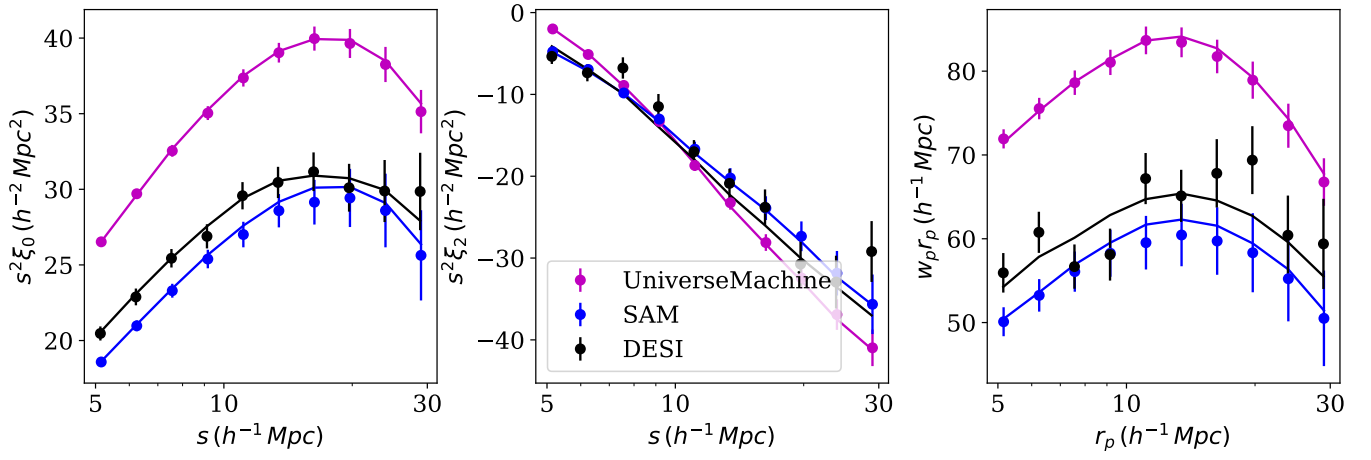


Figure D1. The 2PCF of UniverseMachine ELGs (magenta circles with error bars) at $z = 0.9436$, SAM ELGs (blue circles with error bars) at $z = 0.99$, and DESI ELGs (black circles with error bars) with $z_{\text{eff}} = 0.9565$, and their corresponding best-fitting SHAM galaxies. The 2PCF monopoles, quadrupole and projected 2PCF are presented in the left, middle and right panels respectively.